Ocean Engineering 363 (2026) 126646

Contents lists available at ScienceDirect

Ocean Engineering

journal homepage: www.elsevier.com/locate/oceaneng

Research paper

Hydroelasticity and power capture of raft-type WEC–interconnected VLFS configuration

Haitao Wu [a], Laibing Jia [a], Xiaosen Xu [b], Wanru Deng [c,*], Zhiming Yuan [a,**]

[a] Department of Naval Architecture, Ocean & Marine Engineering, University of Strathclyde, UK
[b] Jiangsu University of Science and Technology, Zhenjiang, China
[c] State Key Laboratory of Hydraulic Engineering Intelligent Construction and Operation, Tianjin University, Tianjin, 300072, China

ARTICLE INFO

Keywords:
Interconnected very large floating structure
Raft-type wave energy converter
PTO system
Hydroelastic response
Power capture performance

ABSTRACT

This paper presents a systematic numerical investigation of the hydroelastic response and energy capture characteristics of raft-type WEC–interconnected very large floating structure (VLFS) system. In the proposed configuration, the WEC is positioned at the fore-end of VLFS, and its power take-off (PTO) mechanism is modeled as a hinge with rotational damping. The wave excitation induces the rotational motion around the hinge, which can drive the PTO to absorb the wave energy. Meanwhile, adjacent VLFS modules are connected by hinges with prescribed rotational stiffness, enabling inter-module rotations and thereby representing the global structural flexibility. From a methodological perspective, the VLFS structure is discretized employing the discrete-module–beam bending (DMBB) method, and the motion equation of the system in the frequency domain is formulated with Lagrange multiplier method. A numerical search procedure is further implemented to determine the optimal PTO damping, with the objective of maximizing power capture efficiency. On this basis, a parametric study is utilized to evaluate the influence of wave and system properties. The results demonstrate that variations in wave and system parameters can significantly influence both the deformation of the VLFS and the power capture of the WEC. Overall, the present study provides valuable insights for the structural design and performance optimization of WEC–VLFS systems.

1. Introduction

As a significant alternative to conventional land reclamation, VLFSs have been widely envisioned and applied across a variety of engineering scenarios, including floating bridges, offshore airports, floating photovoltaic (PV) farms, and offshore oil and gas storage and transfer facilities (Lamas-Pardo et al., 2015; Zhang et al., 2026). Given that VLFSs typically possess extremely large horizontal dimensions and small thickness, their elastic deformations under environmental loads are often considerably more pronounced than rigid-body motions. Consequently, the interaction between structural flexibility and the surrounding fluid field emerges as a critical research field that requires in-depth investigation—namely, the hydroelastic problem. Accurate characterization and analysis of this phenomenon are essential for reliably predicting the overall dynamic response of VLFSs and for guiding their optimized design, carrying both significant theoretical implications and practical engineering value.

So far, several numerical approaches have been developed to investigate the hydroelasticity of flexible structures under wave excitation, which can be broadly classified into three categories: modal superposition method, direct method, and DMBB method. In the modal superposition approach, a systematic modal analysis of the structure is first conducted to extract a sufficient number of rigid-body and elastic modes, after which the overall hydroelastic response is obtained by linearly superimposing the responses of all relevant modes (Senjanović et al., 2008; Michailides et al., 2013). This method is theoretically rigorous; however, its accuracy depends strongly on the adequacy of mode truncation and the number of modes considered. The direct method, by contrast, constructs a finite element model of the structure and solves the fully coupled system with external hydrodynamic loads to directly obtain the hydroelastic response (Kim et al., 2007; Taylor, 2007). While this approach can comprehensively capture fluid–structure interaction effects, it typically involves the solution of large-scale systems of equations, resulting in high computational cost

* Corresponding author.
** Corresponding author.
E-mail addresses: dengwanru@tju.edu.cn (W. Deng), zhiming.yuan@strath.ac.uk (Z. Yuan).

https://doi.org/10.1016/j.oceaneng.2026.126646
Received 24 March 2026; Received in revised form 14 June 2026; Accepted 18 June 2026
Available online 24 June 2026

and relatively low efficiency. The DMBB method, in comparison, discretizes a continuous flexible structure into multiple rigid submodules connected via Euler–Bernoulli beam elements to represent bending deformations (Zhang et al., 2018; Chen et al., 2022; Zhao et al., 2023; Jin et al., 2025). This method does not require prior modal analysis nor the construction of a full finite element model, and it generally achieves favorable computational efficiency while maintaining adequate accuracy, making it highly attractive for practical engineering applications. In addition to the three mainstream approaches mentioned above, researchers have also developed several complementary methods, including the discrete–module–finite element method (Chen et al., 2023; Shi et al., 2024) and semi-analytical approaches (Kashiwagi, 2000; Belibassakis and Athanassoulis, 2005; Papathanasiou et al., 2015). These techniques characterize the hydroelastic response of flexible structures from different perspectives, thereby further enriching the theoretical and numerical analysis framework in this field.

For most engineering applications, the operational performance and structural safety of VLFSs are closely related to their hydroelastic response under wave action, making effective mitigation of such responses of significant engineering and research importance. A range of control and optimization strategies has been proposed to reduce the bending deflections induced in flexible structures by wave excitation (Wang et al., 2010). The most traditional and straightforward approach involves increasing the overall structural stiffness to limit deformation responses (Andrianov and Hermans, 2003). However, this strategy typically entails substantial material and construction costs and is often difficult to implement for existing VLFSs, thereby limiting its practical applicability. Beyond stiffness enhancement, researchers have proposed a variety of alternative measures from the perspectives of external hydrodynamic control and structural dynamic optimization. These include: deploying breakwaters to attenuate incident wave energy (Hong et al., 2006; Diamantoulaki et al., 2008; Loukogeorgaki et al., 2012); installing submerged motion-restraining devices to enhance fluid damping effects (Pham et al., 2008; Cheng et al., 2016; Nguyen et al., 2023); configuring mooring systems to constrain overall structural motions (Zhao et al., 2007; Karmakar and Guedes Soares, 2012; Karperaki et al., 2016); optimizing the structure's shape to improve hydrodynamic performance (Kim et al., 2005; Tay and Wang, 2012); and introducing semi-rigid connections within the structure to regulate the global distribution of flexibility and stiffness (Riyansyah et al., 2010; Gao et al., 2011; Yoon et al., 2014).

From another perspective, ocean waves contain vast energy resources. Integrating WECs into VLFS systems, simultaneously mitigating hydroelastic responses while enabling energy extraction, has emerged as a promising solution that combines structural control with renewable energy utilization. Moreover, the harvested wave energy can provide a continuous power supply for onboard equipment, thereby enhancing the overall energy self-sufficiency of VLFS platforms (Zhang et al., 2019). Motivated by this concept, many scholars have focused on exploring various configurations of integrated WEC–VLFS systems and conducting systematic numerical investigations into their hydroelastic behavior. Nguyen and Wang (2020) proposed a configuration in which heaving-type WECs are mounted on a pontoon-type VLFS. In this system, each PTO unit is connected to the VLFS at one end and anchored to the seabed at the other. The results showed that, compared with previously proposed WEC–VLFS systems (Nguyen et al., 2019), this configuration exhibits superior energy capture performance under long-wave and large oblique wave conditions. Cheng et al. (2023) designed an integrated system where several oscillating water column (OWC) devices, combined with oscillating flaps, are arranged along the weather side of a VLFS. The numerical results indicated that the addition of oscillating flaps at the bottom of the OWC walls can further reduce the hydroelastic response of the structure; moreover, when the flaps are installed on the rear wall, the energy capture efficiency is significantly enhanced. Tay (2025) introduced a design concept that integrates raft-type modular WECs with a large floating PV platform, aiming to simultaneously suppress structural responses and improve energy harvesting performance. Numerical simulations demonstrated that optimizing the WEC length can increase wave energy absorption efficiency by at least 30%, while effectively reducing structural deformations. Zhao et al. (2026) investigated an oscillating-body WEC–VLFS coupled system, systematically examining the influence of key physical parameters on hydroelastic responses and energy capture efficiency. Based on an efficient hydroelastic analysis model developed from the potential flow model, the numerical results revealed that neglecting hydroelastic effects may lead to significant overestimation of energy capture efficiency in the low-frequency range. Wu and Yuan (2026a) proposed an integrated concept combining modular WECs with interconnected VLFS and established a hydroelastic model to study the effects of WEC geometries on system behavior. The findings indicated that, among various design parameters, the WEC length exhibits the most pronounced effects on both global structural response and energy absorption efficiency. Furthermore, the incorporation of WECs was found to be particularly effective in suppressing structural deformations under short-wave conditions.

Building upon the previous study (Wu and Yuan, 2026a), the present work extends the investigation by shifting the research focus from WEC geometric parameters to key system properties of the VLFS. For the proposed raft-type WEC–interconnected VLFS system, the DMBB method is employed to achieve a modular discretization of the structure, while the governing equation of motion in the frequency domain are formulated using the Lagrange multiplier method. On this basis, a numerical search strategy is implemented to determine the optimal PTO damping, with the aim of achieving optimal energy capture performance. Subsequently, a comprehensive parametric study is conducted with respect to both wave and system properties. Particular attention is given to the effects of wave incident angle, structural flexibility, hinge rotational stiffness, hinge location, and the number of hinges on the hydroelasticity and energy absorption. By integrating the present study with prior work (Wu and Yuan, 2026a), a systematic investigation of the WEC–VLFS system is carried out from two complementary perspectives, namely “WEC parameters” and “VLFS properties.” The findings are expected to provide valuable insights into the design optimization and performance evaluation of other types of WEC–VLFS systems.

2. Theoretical background

2.1. Description of raft-type WEC-interconnected VLFS integrated system

Fig. 1 illustrates an illustration of the raft-type WEC–interconnected VLFS configuration, in which the variables of the key system properties are also defined. Both the relative rotation between adjacent VLFS modules, and the relative rotation between the WEC and the fore-end of the VLFS are assumed to occur only about the y-axis; that is, the hinge connections release solely the rotational degree of freedom (DoF) in pitch. A PTO system is installed at the hinge connecting the WEC and the VLFS, enabling electricity generation through their wave-induced relative rotation about the y-axis. Among various PTO configurations, hydraulic systems are the most commonly adopted in practice. In the present study, the PTO damping coefficient C_p is assumed to be constant. This simplification has also been adopted in other studies (Zheng et al., 2015; Zhang et al., 2019; Wu and Yuan, 2026b), thereby allowing the application of frequency-domain analysis. For the numerical modeling of multi-hinged VLFS configurations, the formulation can be readily extended based on the methodology developed for the single-hinged VLFS described in this section.

2.2. Frequency-domain motion equation

In this study, the hydroelastic response of the VLFS is evaluated using the DMBB method, which effectively couples multibody hydrodynamics and structural dynamics based on potential flow theory and

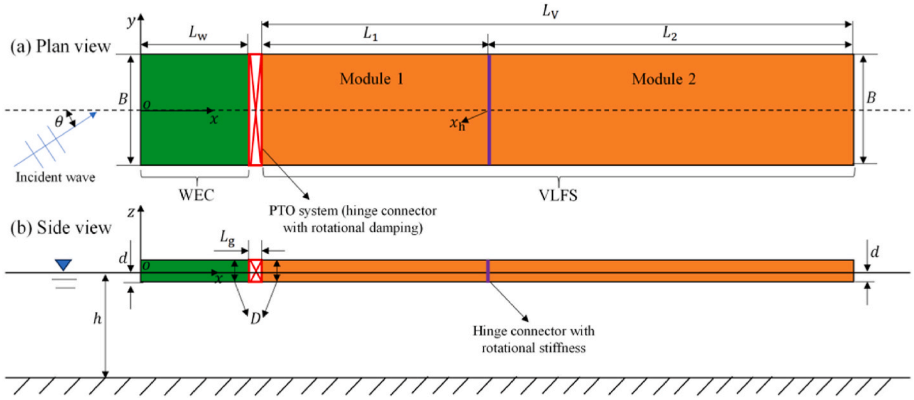

Fig. 1. An illustration of raft-type WEC-interconnected VLFS configuration.

Euler–Bernoulli beam theory, respectively. Firstly, the VLFS fore and aft modules are discretized into N_1 and N_2 rigid submodules, respectively. The hydrodynamic coefficients and wave excitation forces acting on these submodules are then computed within potential flow framework. Subsequently, each submodule is treated as a lumped mass concentrated at its center of gravity (CoG), and the structural deformation is determined by connecting adjacent submodules with equivalent Euler–Bernoulli beam elements. Further details regarding the implementation of the DMBB method can be found in the work of Lu et al. (2019).

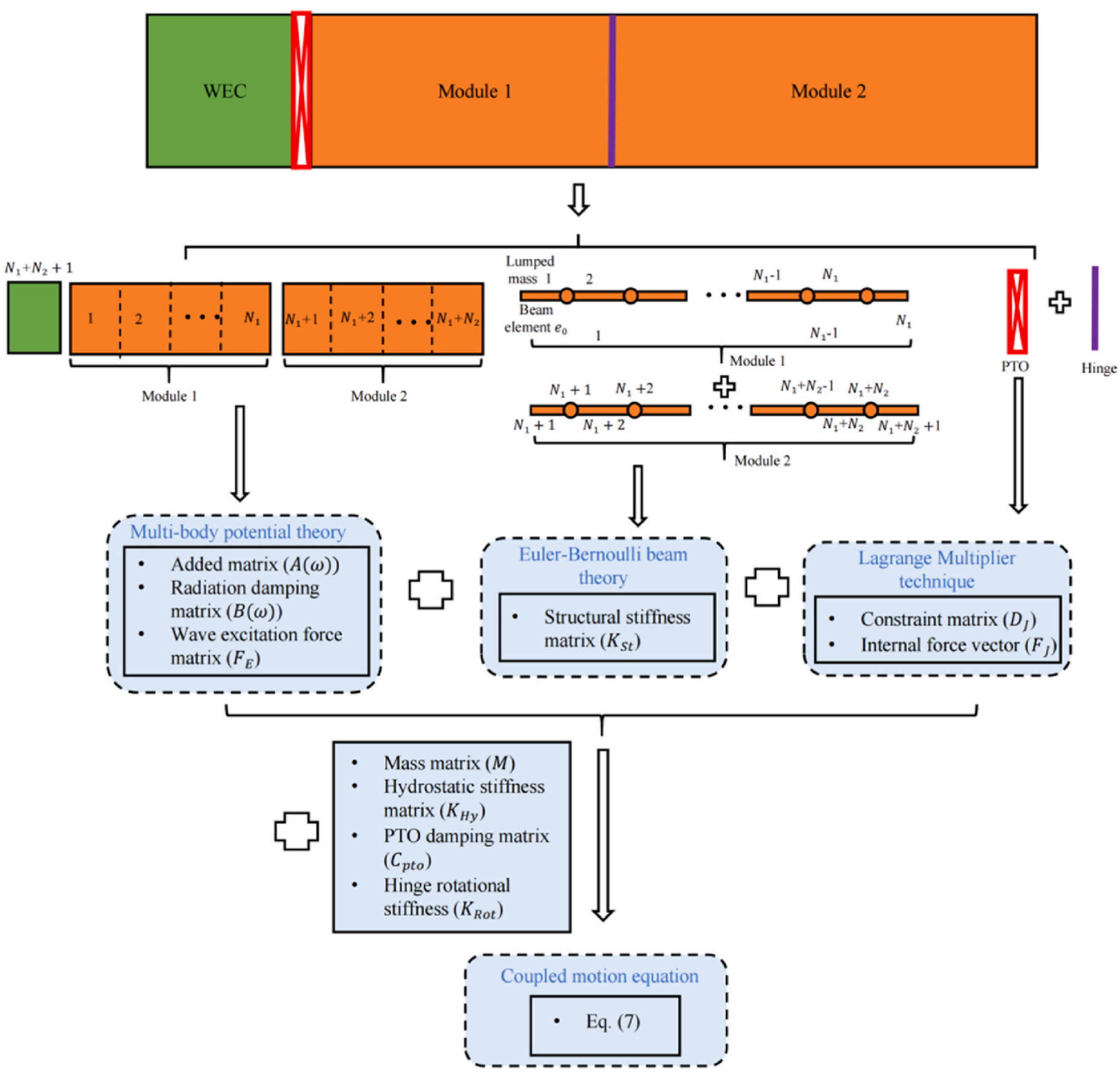

Fig. 2. An illustration of hydroelastic analysis procedure based on the DMBB method.

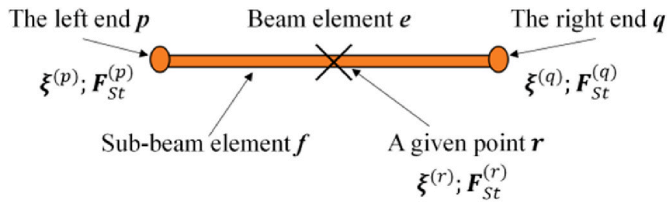

Fig. 3. An illustration of hydroelastic response calculation.

As for the hinge connections between the two VLFS modules and between the WEC and the first submodule of the VLFS, they are numerically modeled using the Lagrange multiplier method. The WEC is assumed to be the $N_1 + N_2 + 1$-th body. As previously stated, the two bodies connected by a hinge are only allowed to undergo relative rotation about the *y*-axis. Accordingly, the displacement continuity conditions imposed by these two hinge constraints can be expressed as follows:

$$\begin{cases} \xi_1^{(1)} = \xi_1^{(N_1+N_2+1)} \\ \xi_2^{(1)} - \left(\dfrac{L_1}{2N_1} + \dfrac{L_g}{2}\right)\xi_6^{(1)} = \xi_2^{(N_1+N_2+1)} + \left(\dfrac{L_w}{2} + \dfrac{L_g}{2}\right)\xi_6^{(N_1+N_2+1)} \\ \xi_3^{(1)} + \left(\dfrac{L_1}{2N_1} + \dfrac{L_g}{2}\right)\xi_5^{(1)} = \xi_3^{(N_1+N_2+1)} - \left(\dfrac{L_w}{2} + \dfrac{L_g}{2}\right)\xi_5^{(N_1+N_2+1)} \\ \xi_4^{(1)} = \xi_4^{(N_1+N_2+1)} \\ \xi_6^{(1)} = \xi_6^{(N_1+N_2+1)} \end{cases} \tag{1}$$

$$\begin{cases} \xi_1^{(N_1)} = \xi_1^{(N_1+1)} \\ \xi_2^{(N_1)} + \dfrac{L_1}{2N_1}\xi_6^{(N_1)} = \xi_2^{(N_1+1)} - \dfrac{L_2}{2N_2}\xi_6^{(N_1+1)} \\ \xi_3^{(N_1)} - \dfrac{L_1}{2N_1}\xi_5^{(N_1)} = \xi_3^{(N_1+1)} + \dfrac{L_2}{2N_2}\xi_5^{(N_1+1)} \\ \xi_4^{(N_1)} = \xi_4^{(N_1+1)} \\ \xi_6^{(N_1)} = \xi_6^{(N_1+1)} \end{cases} \tag{2}$$

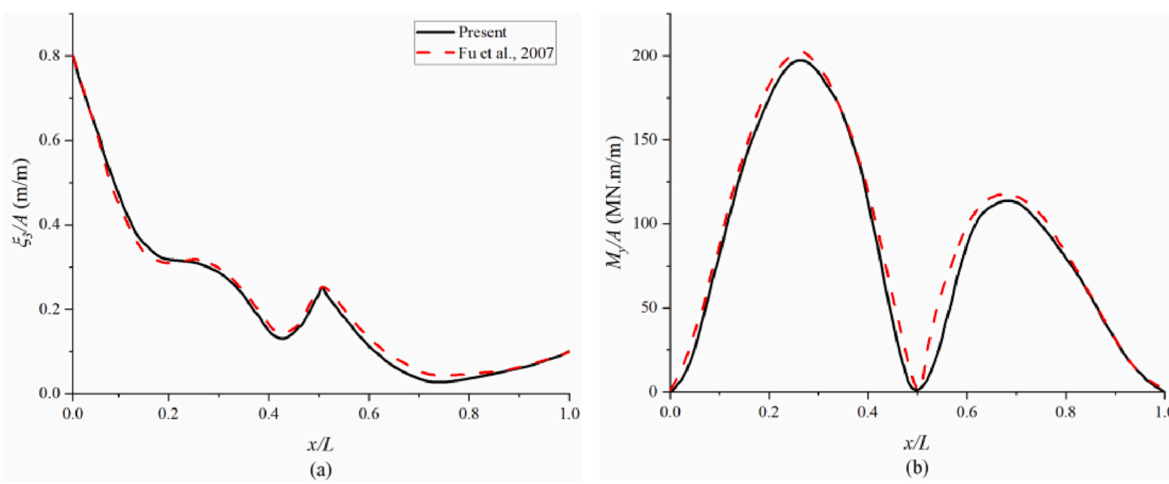

Fig. 4. Comparison of hydroelastic responses between the present and the prior studies: (a) vertical displacement at a wavelength of $\lambda = 120$ m; (b) vertical bending moment at a wavelength of $\lambda = 144$ m.

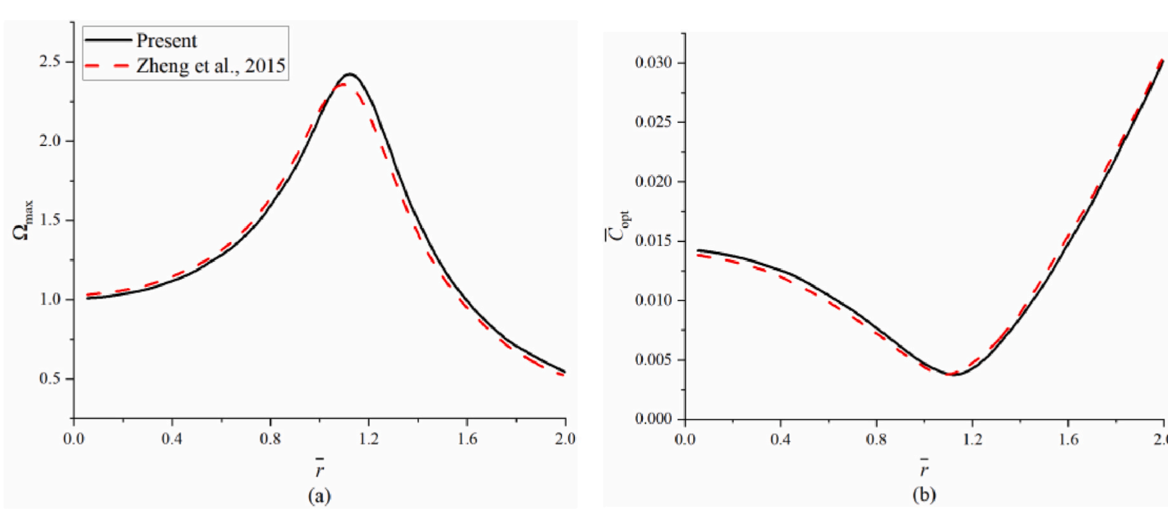

Fig. 5. Comparison of the dimensionless results between the present and the prior studies: (a) maximum CWR; (b) optimal PTO damping.

It's worth noting that, $\boldsymbol{\xi}^{(j)} = \left[\xi_1^{(j)}\ \xi_2^{(j)}\ \xi_3^{(j)}\ \xi_4^{(j)}\ \xi_5^{(j)}\ \xi_6^{(j)}\right]^T$ is the complex displacement of thej-th body, where $\xi_i^{(j)}(i=1,2,3)$ is the translational displacement along the *x*, *y* and *z*-axis, and $\xi_i^{(j)}(i=4,5,6)$ is the rotational displacement around the *x*, *y* and *z*-axis.

Eqs. (1) and (2) can be assembled to form the global constraint matrix of the entire system,

$$\mathbf{D}_J = \begin{bmatrix} \mathbf{D}^{(1)} & 0_{5\times 6(N_1+N_2-1)} & \mathbf{D}^{(N_1+N_2+1)} & \\ 0_{5\times 6(N_1-1)} & \mathbf{D}^{(N_1)} & \mathbf{D}^{(N_1+1)} & 0_{5\times 6N_2} \end{bmatrix} \tag{3}$$

where $\mathbf{D}^{(1)}$, $D^{(N_1+N_2+1)}$, $D^{(N_1)}$ and $\mathbf{D}^{(N_1+1)}$ are all matrices of dimension 5 × 6,

$$\left[\mathbf{D}^{(1)}\quad \mathbf{D}^{(N_1+N_2+1)}\right] = \begin{bmatrix} 1 & 0 & 0 & 0 & 0 & 0 & -1 & 0 & 0 & 0 & 0 & 0 \\ 0 & 1 & 0 & 0 & 0 & -\left(\frac{L_1}{2N_1}+\frac{L_g}{2}\right) & 0 & -1 & 0 & 0 & 0 & -\left(\frac{L_w}{2}+\frac{L_g}{2}\right) \\ 0 & 0 & 1 & 0 & \left(\frac{L_1}{2N_1}+\frac{L_g}{2}\right) & 0 & 0 & 0 & -1 & 0 & \left(\frac{L_w}{2}+\frac{L_g}{2}\right) & 0 \\ 0 & 0 & 0 & 1 & 0 & 0 & 0 & 0 & 0 & -1 & 0 & 0 \\ 0 & 0 & 0 & 0 & 0 & 1 & 0 & 0 & 0 & 0 & 0 & -1 \end{bmatrix} \tag{4}$$

$$\left[\mathbf{D}^{(N_1)}\quad \mathbf{D}^{(N_1+1)}\right] = \begin{bmatrix} 1 & 0 & 0 & 0 & 0 & 0 & -1 & 0 & 0 & 0 & 0 & 0 \\ 0 & 1 & 0 & 0 & 0 & \frac{L_1}{2N_1} & 0 & -1 & 0 & 0 & 0 & \frac{L_2}{2N_2} \\ 0 & 0 & 1 & 0 & -\frac{L_1}{2N_1} & 0 & 0 & 0 & -1 & 0 & -\frac{L_2}{2N_2} & 0 \\ 0 & 0 & 0 & 1 & 0 & 0 & 0 & 0 & 0 & -1 & 0 & 0 \\ 0 & 0 & 0 & 0 & 0 & 1 & 0 & 0 & 0 & 0 & 0 & -1 \end{bmatrix} \tag{5}$$

The internal force vector associated with the two hinges can be expressed as:

$$\mathbf{F}_J = \left[\mathbf{F}_J^{(1,N_1+N_2+1)}\quad \mathbf{F}_J^{(N_1,N_1+1)}\right]^T \tag{6}$$

where $\mathbf{F}_J^{(1,N_1+N_2+1)} = \left[F_{J1}^{(1,N_1+N_2+1)}\ F_{J2}^{(1,N_1+N_2+1)}\ F_{J3}^{(1,N_1+N_2+1)}\ F_{J4}^{(1,N_1+N_2+1)}\ F_{J6}^{(1,N_1+N_2+1)}\right]$ and $\mathbf{F}_J^{(N_1,N_1+1)} = \left[F_{J1}^{(N_1,N_1+1)}\ F_{J2}^{(N_1,N_1+1)}\ F_{J3}^{(N_1,N_1+1)}\ F_{J4}^{(N_1,N_1+1)}\ F_{J6}^{(N_1,N_1+1)}\right]$ correspond to the hinge between the WEC and the first VLFS submodule, and the hinge between the two VLFS modules, respectively. $F_{Ji}(i=1,2,3)$ represent the forces along the *x*, *y* and *z*-axis, while $F_{Ji}(i=4,6)$ denote the moments about the *x*- and *z*-axis. During the hydroelastic analysis, the hinge internal force vector is converted into equivalent external forces acting at the CoGs of the adjacent bodies using the formula $\mathbf{D}_J^T\mathbf{F}_J$ (Sun et al., 2011).

Finally, on the basis of DMBB and Lagrange multiplier methods described above, the motion equation for the system in the frequency domain can be expressed as follows:

$$\begin{bmatrix} -\omega^2(\mathbf{M}+\mathbf{A}(\omega)) + i\omega(\mathbf{B}(\omega)+\mathbf{C}_{pto}) + \mathbf{K}_{Hy} + \mathbf{K}_{Rot} + \mathbf{K}_{St} & \mathbf{D}_J^T \\ \mathbf{D}_J & 0 \end{bmatrix} \begin{bmatrix} \boldsymbol{\xi} \\ \mathbf{F}_J \end{bmatrix} = \begin{bmatrix} \mathbf{F}_E \\ 0 \end{bmatrix} \tag{7}$$

where $\mathbf{M}$ is the mass matrix; $\mathbf{A}(\omega)$ and $\mathbf{B}(\omega)$ are the added mass and radiation damping matrices at the wave frequency ω, respectively; $\mathbf{K}_{Hy}$, $\mathbf{K}_{Rot}$, and $\mathbf{K}_{St}$ denote the hydrostatic stiffness, hinge rotational stiffness, and structural stiffness matrices, respectively; $\mathbf{C}_{pto}$ is the PTO damping matrix; $\boldsymbol{\xi}$ and $\mathbf{F}_E$ are the displacement and wave excitation force vectors. The expression forms of these vectors and matrices are given in Appendix A. Meanwhile, a schematic illustration of the hydroelastic analysis procedure using this approach is presented in Fig. 2. Specifically, the numbering of all submodules and beam elements is indicated in the figure.

After solving Eq. (7) to obtain the displacement responses of each body, the power captured by the WEC can be calculated using the following formula,

$$P_w = \frac{1}{2}C_p\omega^2\left|\xi_5^{(N_1+N_2+1)} - \xi_5^{(1)}\right|^2 \tag{8}$$

Accordingly, the capture width ratio (CWR) of the WEC can be defined as:

$$\Omega = \frac{P_w}{d_e P_I} \tag{9}$$

where d_e denotes the effective width of the WEC in the wave incident angle; P_I represents the incident wave power per unit width.

$$P_I = \frac{\rho g A^2\omega}{4k}\left(1+\frac{2kh}{\sinh(2kh)}\right) \tag{10}$$

where ρ is the density of seawater; g is the gravitational acceleration; A and k denote the wave amplitude and wave number of the incident wave, respectively; h is the water depth. Under finite water depth condition, ω and k can be related by the following formula:

$$\omega^2 = gk\tanh kh \tag{11}$$

2.3. Calculation of hydroelastic response

After solving Eq. (7), the displacements of all lumped masses on the VLFS are obtained. Based on the structural stiffness matrix of any beam element, $\mathbf{K}_e$ (see Appendix A), the forces at the element ends induced from structural deformation can then be computed. Fig. 3 illustrates the displacements of the lumped masses p and q ($\boldsymbol{\xi}^{(p)}$ and $\boldsymbol{\xi}^{(q)}$) at the ends of beam element e and the induced structural forces ($\mathbf{F}_{St}^{(p)}$ and $\mathbf{F}_{St}^{(p)}$). The structural forces can be calculated as follows:

$$\begin{bmatrix}\mathbf{F}_{St}^{(p)}\\ \mathbf{F}_{St}^{(q)}\end{bmatrix}=\mathbf{K}_e\begin{bmatrix}\boldsymbol{\xi}^{(p)}\\ \boldsymbol{\xi}^{(q)}\end{bmatrix}=\begin{bmatrix}\mathbf{K}_e^{(p,p)} & \mathbf{K}_e^{(p,q)}\\ \mathbf{K}_e^{(q,p)} & \mathbf{K}_e^{(q,q)}\end{bmatrix}\begin{bmatrix}\boldsymbol{\xi}^{(p)}\\ \boldsymbol{\xi}^{(q)}\end{bmatrix} \tag{12}$$

where $\mathbf{K}_e^{(p,p)}$, $\mathbf{K}_e^{(p,q)}$, $\mathbf{K}_e^{(q,p)}$ and $\mathbf{K}_e^{(q,q)}$ are the four submatrices of $\mathbf{K}_e$ with the dimension of 6×6.

In addition, the figure also indicates a given point r along beam element e. Formed between the left end p and point r, the stiffness matrix of the sub-beam element f is defined as $\mathbf{K}_f$, which has the same dimensions as $\mathbf{K}_e$. The displacement and structural force at point r can then be related as follows:

$$\begin{bmatrix}\mathbf{F}_{St}^{(p)}\\ \mathbf{F}_{St}^{(r)}\end{bmatrix}=\mathbf{K}_f\begin{bmatrix}\boldsymbol{\xi}^{(p)}\\ \boldsymbol{\xi}^{(r)}\end{bmatrix}=\begin{bmatrix}\mathbf{K}_f^{(p,p)} & \mathbf{K}_f^{(p,r)}\\ \mathbf{K}_f^{(r,p)} & \mathbf{K}_f^{(r,r)}\end{bmatrix}\begin{bmatrix}\boldsymbol{\xi}^{(p)}\\ \boldsymbol{\xi}^{(r)}\end{bmatrix} \tag{13}$$

After manipulation of Eq. (13), the displacement and structural force at point r can be obtained,

$$\boldsymbol{\xi}^{(r)}=\left[\mathbf{K}_f^{(p,r)}\right]^{-1}\left[\mathbf{F}_{St}^{(p)}-\mathbf{K}_f^{(p,p)}\boldsymbol{\xi}^{(p)}\right] \tag{14}$$

$$\mathbf{F}_{St}^{(r)}=\mathbf{K}_f^{(r,p)}\boldsymbol{\xi}^{(p)}+\mathbf{K}_f^{(r,r)}\left[\mathbf{K}_f^{(p,r)}\right]^{-1}\left(\mathbf{F}_{St}^{(p)}-\mathbf{K}_f^{(p,p)}\boldsymbol{\xi}^{(p)}\right) \tag{15}$$

As pointed out by Sun et al. (2018), the structural forces obtained from Eq. (15) are accurate only at the interfaces between adjacent submodules. Therefore, once the interface forces are obtained, a high-order interpolation scheme, as proposed by Sun et al. (2018), can be employed to evaluate the structural forces at arbitrary locations along the VLFS. Denoting the longitudinal coordinates of the left and right interfaces of a submodule as x_i and x_{i+1}, and the corresponding vertical bending moment and shear force as M_i, N_i, and M_{i+1}, N_{i+1}, the interpolation function for the vertical bending moment along this submodule can be expressed as:

$$M(x)=a_1+a_2x+a_3x^2+a_4x^3 \tag{16a}$$

Based on the relationship between bending moment and shear force in Euler–Bernoulli beam theory, substituting the position coordinates and structural forces at both ends of this submodule into Eq. (16) yields:

$$\begin{bmatrix}1 & x_i & x_i^2 & x_i^3\\ 1 & x_{i+1} & x_{i+1}^2 & x_{i+1}^3\\ 0 & 1 & 2x_i & 3x_i^2\\ 0 & 1 & 2x_{i+1} & 3x_{i+1}^2\end{bmatrix}\begin{bmatrix}a_1\\ a_2\\ a_3\\ a_4\end{bmatrix}=\begin{bmatrix}M_i\\ M_{i+1}\\ N_i\\ N_{i+1}\end{bmatrix} \tag{17}$$

By manipulating Eq. (17), the four constant coefficients in Eq. (16) can be determined,

$$\begin{bmatrix}a_1\\ a_2\\ a_3\\ a_4\end{bmatrix}=\begin{bmatrix}1 & x_i & x_i^2 & x_i^3\\ 1 & x_{i+1} & x_{i+1}^2 & x_{i+1}^3\\ 0 & 1 & 2x_i & 3x_i^2\\ 0 & 1 & 2x_{i+1} & 3x_{i+1}^2\end{bmatrix}^{-1}\begin{bmatrix}M_i\\ M_{i+1}\\ N_i\\ N_{i+1}\end{bmatrix} \tag{16b}$$

Finally, it should be emphasized that the hydroelastic response considered in this study involves two quantities: the vertical displacement $\xi_3^{(r)}$ and the vertical bending moment $M_y = F_{St5}^{(r)}$, of which the dimensionless forms can be expressed as $\xi_3^{(r)}/A$ and $M_y(L_w+L_v)^2/(EIA)$, respectively.

3. Validation of the numerical model

This paper employs the DMBB method in combination with the Lagrange multiplier method to perform numerical analysis of the WEC–VLFS configuration. To ensure the accuracy of the present study, both methods need to be validated. A VLFS model composed of two connected modules, with a hinge of zero rotational stiffness at the middle (Fu et al., 2007), is considered as the validation case, of which the length is 300 m, the width is 60 m, and the depth and draft are 2 m and 0.5 m, respectively. Fu et al. (2007) previously computed the hydroelastic response of this model using the conventional modal superposition method. Fig. 4 shows the hydroelastic responses in the present study, exhibiting good agreement with those of Fu et al.

Furthermore, since this system is relatively complex, it is difficult to derive an explicit analytical expression for the optimal PTO damping coefficient. Therefore, the present study employs a numerical search method to determine the optimal PTO damping. The procedure can be briefly described as follows: In the first iteration, the PTO damping range $[0, C_{max}]$ is adopted as the search domain. To ensure that the optimal PTO damping is not excluded, C_{max} should be assigned a sufficiently large value (e.g., 10^{11}). This interval is uniformly divided into m_b subintervals with a step size of ΔC_1, where the subscript "1" denotes the first iteration. The resulting $(n_b + 1)$ PTO damping values are then substituted into Eqs. (7) and (8) to compute (n_b+1) corresponding total power outputs of the WEC. These values are compared to identify the maximum, denoted as $P_{max,1}$, and the corresponding PTO damping is denoted as $C_{p,1}$. In the second iteration, the search domain is refined to $[C_{p,1}-\Delta C_1,\ C_{p,1}+\Delta C_1]$, which is again uniformly divided into m_b subintervals with a step size of ΔC_2. The same procedure is repeated to obtain $P_{max,2}$. This iterative process continues for n iterations until the convergence criterion $|P_{max,n}-P_{max,n\text{-}1}|<\varepsilon$ is satisfied, where ε is a small positive number (e.g., 10^{-6}). The final value $C_{p,n}$ is then taken as the optimal PTO damping, denoted as C_{opt}.

To ensure the accuracy of the current study, the raft-type twin-body WEC model studied by Zheng et al. (2015) is employed to validate this search approach. The model consists of two identical elliptical cylinders separated by a distance of 1 m. Each cylinder has a length of 20 m, a major axis of 5 m, a minor axis of 2.5 m, and a mass of 100629 kg. Assuming a rigid-body behavior, Zheng et al. analyzes the maximum capture width ratio (CWR) (Ω_{max}) and the optimal dimensionless PTO damping ($\overline{C}_{opt}$) of this WEC model at various dimensionless radius of gyration ($\bar{r}$). Since the present model with eight identical submodules accounts for structural flexibility, a sufficiently large structural stiffness is prescribed in the calculations to satisfy the rigid-body assumption. The results obtained from the numerical search method are shown in Fig. 5. It is evident that the present results are in good agreement with those reported by Zheng et al.

4. Results and discussion

Firstly, the main parameters of the WEC and VLFS are listed in Table 1. Since the gap between the fore-end of the VLFS and the WEC is quite narrow ($L_g = 0.5$ m), the fluid resonance may occur inside. Based on the system parameters, an empirical formula is employed to estimate the natural frequency of fluid motion within the narrow gap (Tan et al., 2017):

$$\omega_n=\sqrt{\frac{g}{d+\frac{L_g(L_w+L_v)}{4(h-d)}}} \tag{19}$$

Thus, for $L_g = 0.5$ m, the natural frequency is 2.38 rad/s, corresponding to a wavelength of $\lambda = 10.9$ m. Compared with the overall dimension of the system, this wavelength is quite short and therefore falls outside the scope of the present study. Moreover, to avoid numerical problems, no mesh discretization is applied at the interfaces between adjacent submodules within the VLFS (Tuitman et al., 2012). It's noteworthy that for a VLFS with the length of 300 m, discreting it into eight identical submodules can ensure the reliability of the numerical study (Lu et al., 2019; Sun et al., 2018; Xu et al., 2017).

Finally, based on the established numerical model, subsections 4.1–4.5 conduct a parametric analysis, with the corresponding parameter settings listed in Table 2. Some typical wavelengths of $\lambda/(L_w + L_v) = 0.2$, 0.4, 0.6, 0.8, 1.0 and 1.4 are selected for investigation, which are also adopted in other studies (Lu et al., 2019; Sun et al., 2018; Xu et al., 2017; Shi et al., 2023). It should be noted that, for each subsection, the optimal PTO damping corresponding to the specific parameters and wave conditions is applied.

4.1. Effects of wave incident angle

Fig. 6 presents the vertical displacement of the VLFS under different wave incident angles. Under short-wave condition $\lambda/(L_w + L_v) = 0.2$, the displacement amplitude is relatively small, but significant local oscillations are observed along the length direction. As the incidence angle increases, the displacement response is significantly amplified, reaching a maximum at $\theta = 60^\circ$. This behavior is primarily attributed to the large phase differences induced by oblique waves at different locations along the structure, which enhance local deformations. As the wavelength increases ($\lambda/(L_w + L_v) = 0.4$ and 0.6), the displacement of the structure increases markedly, exhibiting a pronounced peak in the middle. The presence of a hinge at this location allows relative rotation between the fore and aft modules, thereby accentuating the local response. When the wavelength approaches or equals to the length of the structure ($\lambda/(L_w + L_v) = 0.8$ and 1.0), the structure exhibits overall modular deformation, while the hinge connector partially release bending moments through relative rotation, altering the deformation distribution. Under these conditions, the differences in displacement response between various incident angles are less pronounced compared with the short-wave conditions. Under long-wave condition ($\lambda/(L_w + L_v) = 1.4$), the displacement distribution becomes more uniform, and variations among different incident angles are minimal. The structural response is dominated by entire vertical motion, with relatively small deformation and hinge rotation, resulting in a substantially reduced influence of wave incidence angle.

Table 1
Key parameters of the WEC and VLFS.

	Parameter	Unit	Value
WEC	Gap distance/ L_g	m	0.5
	Water depth/ h	m	60
	Length/ L_v	m	45
	Breadth/ B	m	45
	Depth/ D	m	2.5
	Draft/ d	m	1
	Mass	kg	2.076×10^6
VLFS	Length/ L_w	m	300
	Breadth/ B	m	45
	Depth/ D	m	2.5
	Draft/ d	m	1
	Mass	kg	1.384×10^7
	Vertical bending moment/(*EI*)	$N.m^2$	6.97×10^{11}

Table 2
Parameter settings for subsections 4.1-4.5.

Subsections	Wave incident angle (deg)	Structural flexibility ($EI = 6.97 \times 10^{11} N.m^2$)	Hinge rotational stiffness ($\times 10^{10}$ N m)	Hinge location (x_h/L_v)	Hinge number (N_h)
4.1	0; 30; 45; 60	*EI*	0	0.5	1
4.2	0	0.01 *EI*; 0.1 *EI*; *EI*; 10 *EI*; 100 *EI*	0	0.5	1
4.3	0	*EI*	0; 0.16; 0.48; 0.8	0.5	1
4.4	0	*EI*	0	0.25; 0.5; 0.75	1
4.5	0	*EI*	0	0.5; 0.25, 0.5, 0.75; 0.125, 0.25, 0.375, 0.5, 0.625, 0.75, 0.875	1; 3; 7

Fig. 7 presents the vertical bending moment of the VLFS under different wave incident angles. Due to the hinge located at the midspan of the structure, the bending moment at $x/L_v = 0.5$ is zero, indicating that the hinge effectively releases moment transmission between the fore and aft modules. Under short-wave conditions ($\lambda/(L_w + L_v) = 0.2$), the bending moment exhibits pronounced local oscillations along the structural length, with multiple localized peaks. As the incident angle increases, the bending moment response is significantly amplified, reaching a maximum at $\theta = 60^\circ$. This behavior is primarily attributed to oblique waves generating stronger spatial variations in the loading along the structure, thereby enhancing local deformations. As the wavelength increases ($\lambda/(L_w + L_v) = 0.4$ and 0.6), the bending moment distribution becomes progressively smoother, with distinct peaks appearing at the midspan of each module, while the moment at the hinge location remains minimal. When the wavelength approaches or exceeds the length of the structure ($\lambda/(L_w + L_v) = 0.8$ and 1.0), the bending moment reaches higher amplitudes and exhibits a typical double-peak distribution. Unlike the displacement response, the maximum bending moment at these wavelengths generally occurs in the heading wave ($\theta = 0^\circ$), while larger incident angles reduce the moment levels. This suggests that oblique waves disperse wave energy along the structure, thereby mitigating the overall bending effects. Under long-wave condition ($\lambda/(L_w + L_v) = 1.4$), the bending moment amplitudes decrease substantially, and the differences among various incident angles become less pronounced. At this wavelength, the structural response is dominated by entire vertical motion, with limited bending deformation, resulting in overall lower bending moment levels.

Fig. 8 shows the CWR of the WEC under different wave incident angles. Overall, the CWR decreases noticeably with increasing wavelength, and for most wavelengths, the heading wave ($\theta = 0^\circ$) yields higher values. Under short-wave conditions ($\lambda/(L_w + L_v) = 0.2$), the CWR reaches its maximum at $\theta = 60^\circ$. This is because short waves exhibit strong spatial variations, and oblique waves induce more pronounced phase differences along the structure, enhancing the relative motion of the VLFS and WEC. As the wavelength increases ($\lambda/(L_w + L_v) \geq 0.4$), the CWR in the heading wave gradually becomes dominant, while it decreases markedly with increasing incident angle. This behavior is mainly due to the dispersal of wave energy along the length under oblique waves, which reduces the relative motion of the VLFS and WEC. For even longer waves ($\lambda/(L_w + L_v) \geq 0.8$), the CWR declines substantially and tends to converge across different incident angles. This is because, under long-wave conditions, the system motion is dominated by entire vertical motion, and the relative motion of the WEC and VLFS is weakened.

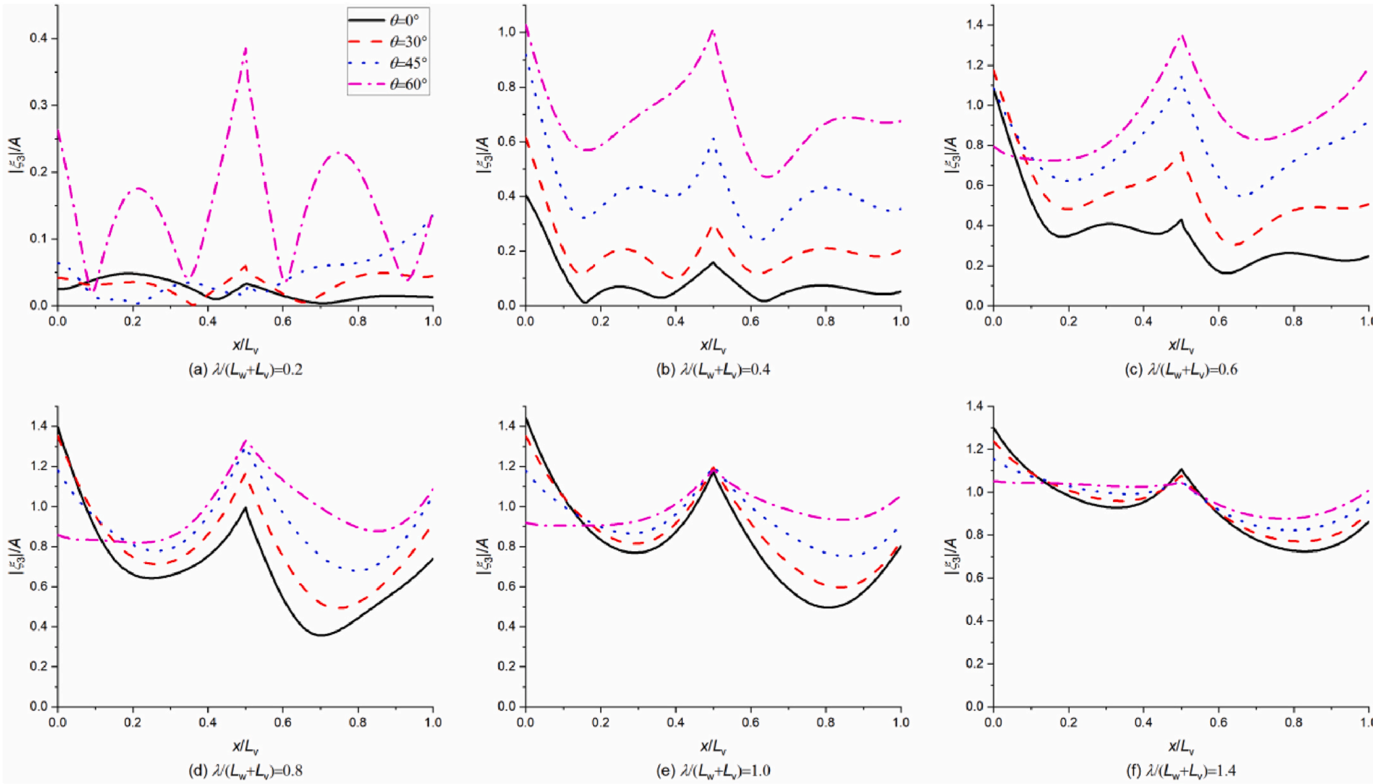

Fig. 6. Vertical displacement of the VLFS under different wave incident angles.

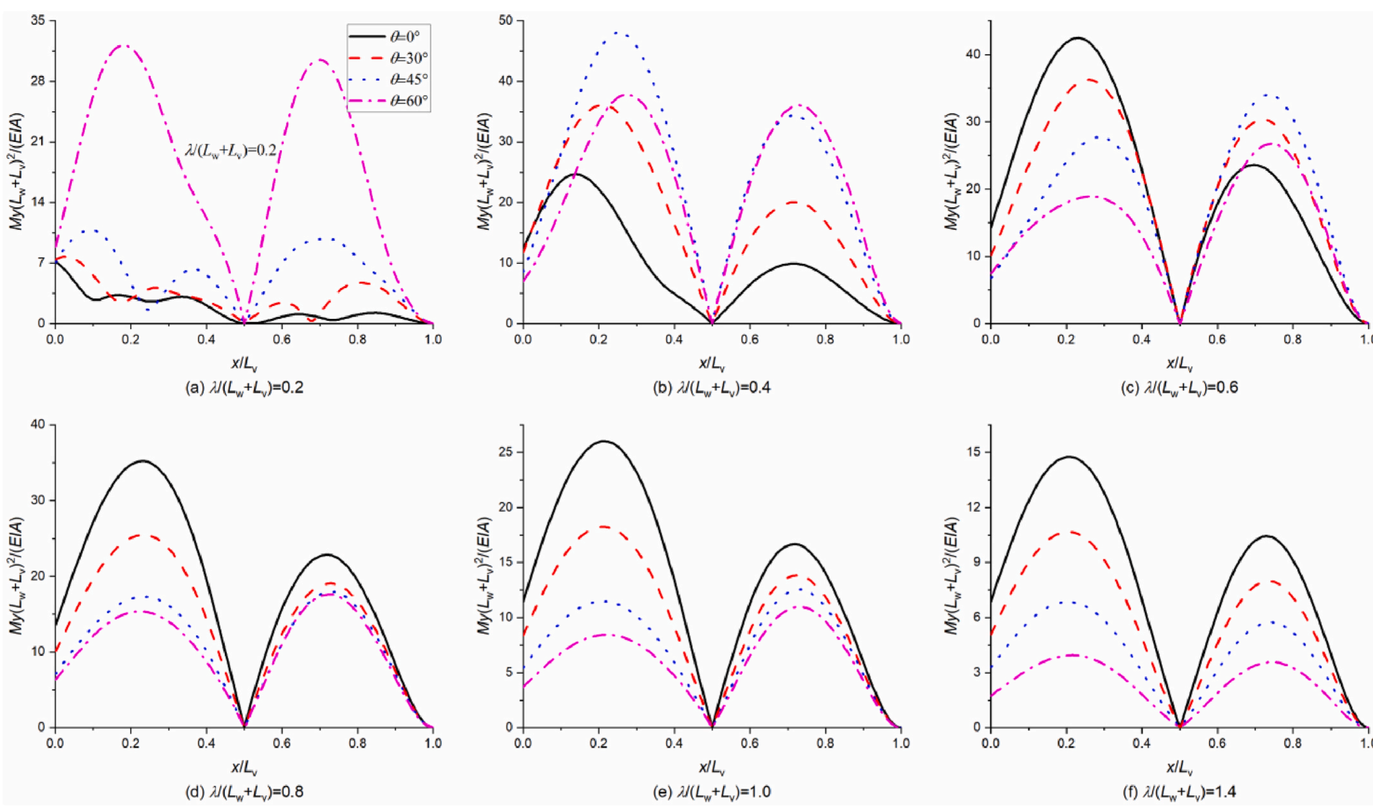

Fig. 7. Vertical bending moment of the VLFS under different wave incident angles.

4.2. Effects of structural flexibility

Fig. 9 presents the vertical displacement of the VLFS with different vertical bending stiffness. Under short-wave conditions ($\lambda/(L_w + L_v) = 0.2$ and 0.4), the overall structural displacement is relatively small but exhibits significant local oscillations. When the bending stiffness is

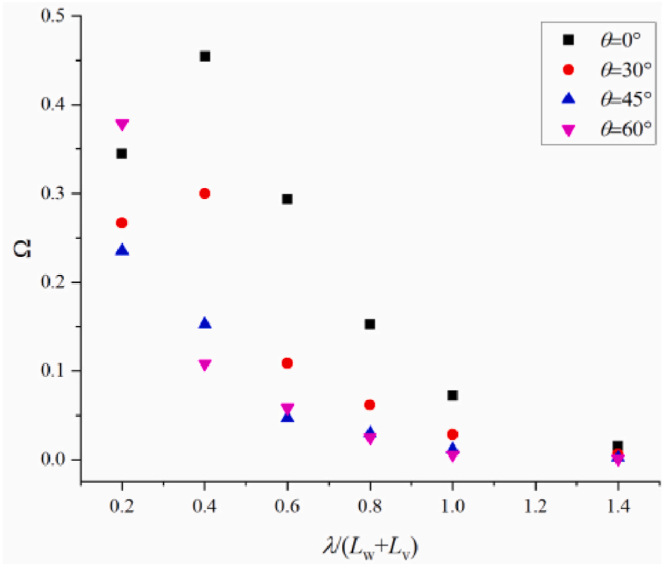

Fig. 8. CWR of the WEC under different wave incident angles.

low, the structure is more susceptible to local bending deformations, resulting in larger displacement amplitudes; as the bending stiffness increases, structural deformations are significantly reduced and the displacement distribution becomes smoother. As the wavelength increases ($\lambda/(L_w + L_v) = 0.6$ and 0.8), the displacement increases markedly, with response peaks appearing near the hinge. This is due to the reduced moment transmission at the hinge, which allows the fore and aft modules to rotate more freely relative to each other. When the wavelength approaches or exceeds the length of the structure ($\lambda/(L_w + L_v) = 1.0$ and 1.4), the displacement response becomes increasingly dominated by entire vertical motion, and the differences among various bending stiffness conditions diminish.

Fig. 10 shows the distribution of vertical bending moment along the longitudinal direction of the VLFS with different vertical bending stiffness. Under short-wave conditions ($\lambda/(L_w + L_v) = 0.2$ and 0.4), the bending moment amplitudes are relatively small overall, but pronounced local variations occur along the structural length. As the bending stiffness increases, the bending moment response is significantly amplified, since stiffer structures deform less under wave action, causing more of the wave energy to be converted into internal forces and thus elevating the bending moment level. With increasing wavelength ($\lambda/(L_w + L_v) = 0.6$ and 0.8), the bending moment distribution gradually develops two distinct peaks located at the midspan of each module, while the moment at the hinge remains close to zero. At these wavelengths, the bending moment amplitude increases noticeably with stiffness, indicating that higher structural rigidity enhances the overall bending response. When the wavelength approaches or exceeds the characteristic length of the structure ($\lambda/(L_w + L_v) = 1.0$ and 1.4), the bending moment distribution exhibits a stable double-peak pattern. Differences among various stiffness conditions remain pronounced, with higher bending stiffness producing larger bending moment responses.

Fig. 11 illustrates the CWR of the WEC under different vertical bending stiffness conditions. Under short-wave conditions ($\lambda/(L_w + L_v) = 0.2$), the WEC achieves its maximum CWR at the lowest bending stiffness (0.01 *EI*), while for the other stiffness values, the CWR gradually increases with increasing bending stiffness. This indicates that, under short waves, more flexible VLFS are prone to local deformations, which enhance the relative motion of the VLFS and WEC. At $\lambda/(L_w + L_v) = 0.4$, the CWR exhibits a different trend with bending stiffness. When the stiffness is greater than or equal to *EI*, the CWR decreases as stiffness increases; whereas for stiffness values below EI, the CWR remains relatively low. This suggests that, at this wavelength, a certain matching exists between the structural stiffness and the wavelengths, which affects the system's energy capture capability. For longer waves ($\lambda/(L_w + L_v) \geq 0.6$), the CWR clearly increases with the bending stiffness.

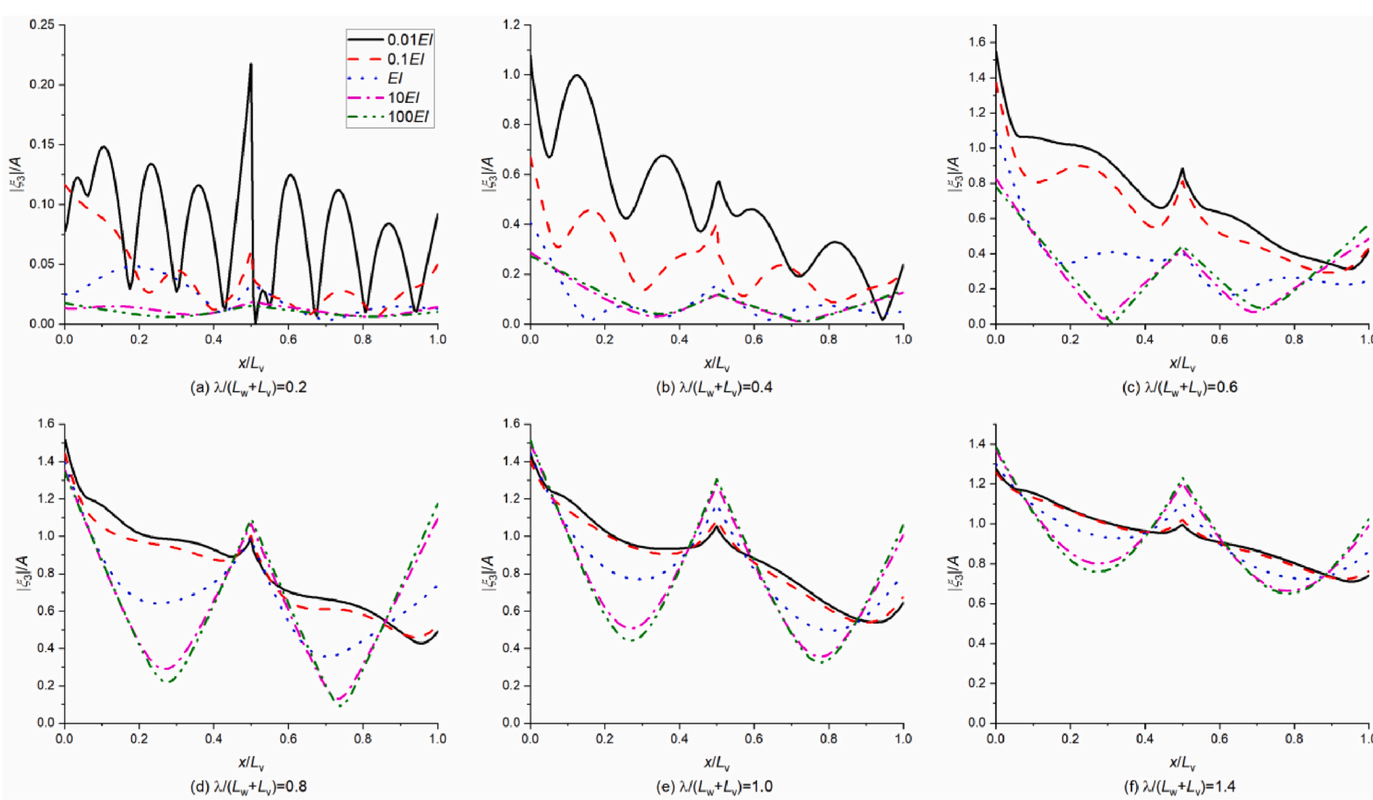

Fig. 9. Vertical displacement of the VLFS with different vertical bending stiffness.

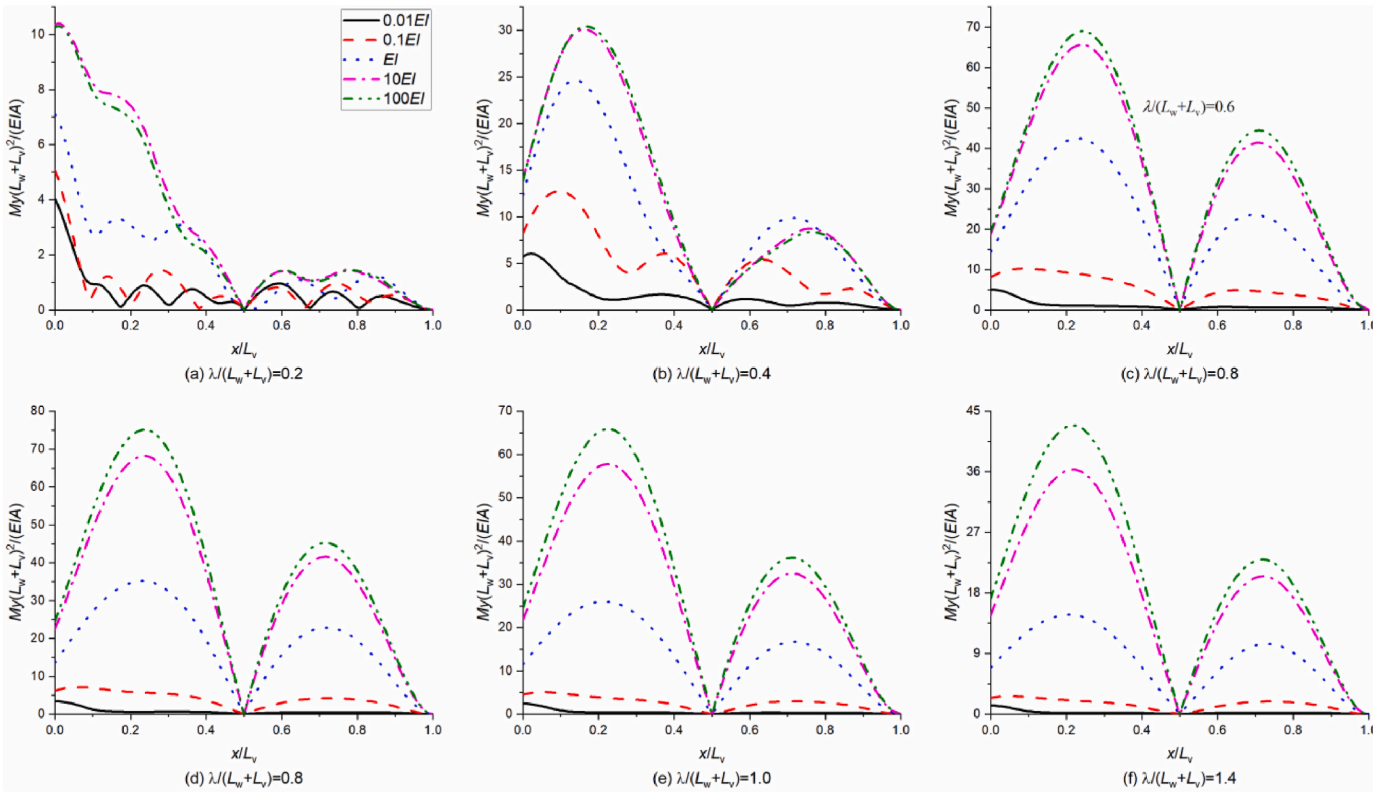

Fig. 10. Vertical bending moment of the VLFS with different vertical bending stiffness.

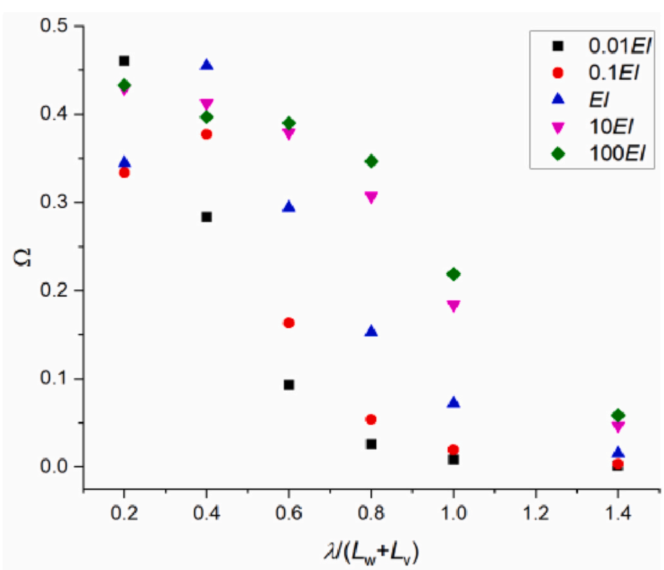

Fig. 11. CWR of the WEC under different vertical bending stiffness conditions.

This is because higher structural stiffness reduces the bending deformation, maintaining more stable relative motion of the VLFS and WEC.

4.3. Effects of hinge rotational stiffness

Fig. 12 presents the vertical displacement of the VLFS under different hinge rotational stiffness conditions. As a hinge connection is introduced at the midspan of the structure, variations in rotational stiffness alter the relative rotational capacity between the fore and aft modules, thereby influencing the overall hydroelastic response. Under short-wave conditions ($\lambda/(L_w + L_v) = 0.2$ and 0.4), the effects of rotational stiffness on the displacement distribution are pronounced. A smaller rotational stiffness allows greater relative rotation at the hinge, resulting in significant local displacement variations in its vicinity. As the rotational stiffness increases, the relative rotation between adjacent modules is progressively constrained, leading to a reduction in peak displacement and a smoother structural response. With increasing wavelength ($\lambda/(L_w + L_v) = 0.6$ and 0.8), the displacement pattern gradually transitions to module-scale global deformation, with peak displacement typically occurring at the hinge location. At these wavelengths, the influence of rotational stiffness becomes less significant; however, higher rotational stiffness still reduces local displacement amplitudes and promotes a more uniform deformation profile. When the wavelength approaches or exceeds the structural scale ($\lambda/(L_w + L_v) = 1.0$ and 1.4), the displacement curves corresponding to different rotational stiffness values nearly coincide. This indicates that the structural response is predominantly governed by entire vertical motion, and the influence of hinge rotational stiffness on the displacement response becomes negligible.

Fig. 13 illustrates the vertical bending moment of the VLFS under different hinge rotational stiffness conditions. At short-wave wavelengths ($\lambda/(L_w + L_v) = 0.2$ and 0.4), the influence of rotational stiffness on the bending moment distribution is significant. A smaller rotational stiffness allows greater relative rotation between the fore and aft modules, thereby alleviating the overall structural bending response. As the rotational stiffness increases, the rotational motion at the hinge is progressively restrained, leading to an enhancement of global bending and an increase in bending moment amplitude. With increasing wavelength ($\lambda/(L_w + L_v) = 0.6$ and 0.8), the bending moment distribution gradually exhibits two distinct peaks, located near the midspan of each module, while the bending moment at the hinge remains minimal. Within this wavelength range, higher rotational stiffness further amplifies the peak bending moments, indicating that restricting hinge rotation intensifies the overall bending response of the structure. When the wavelength

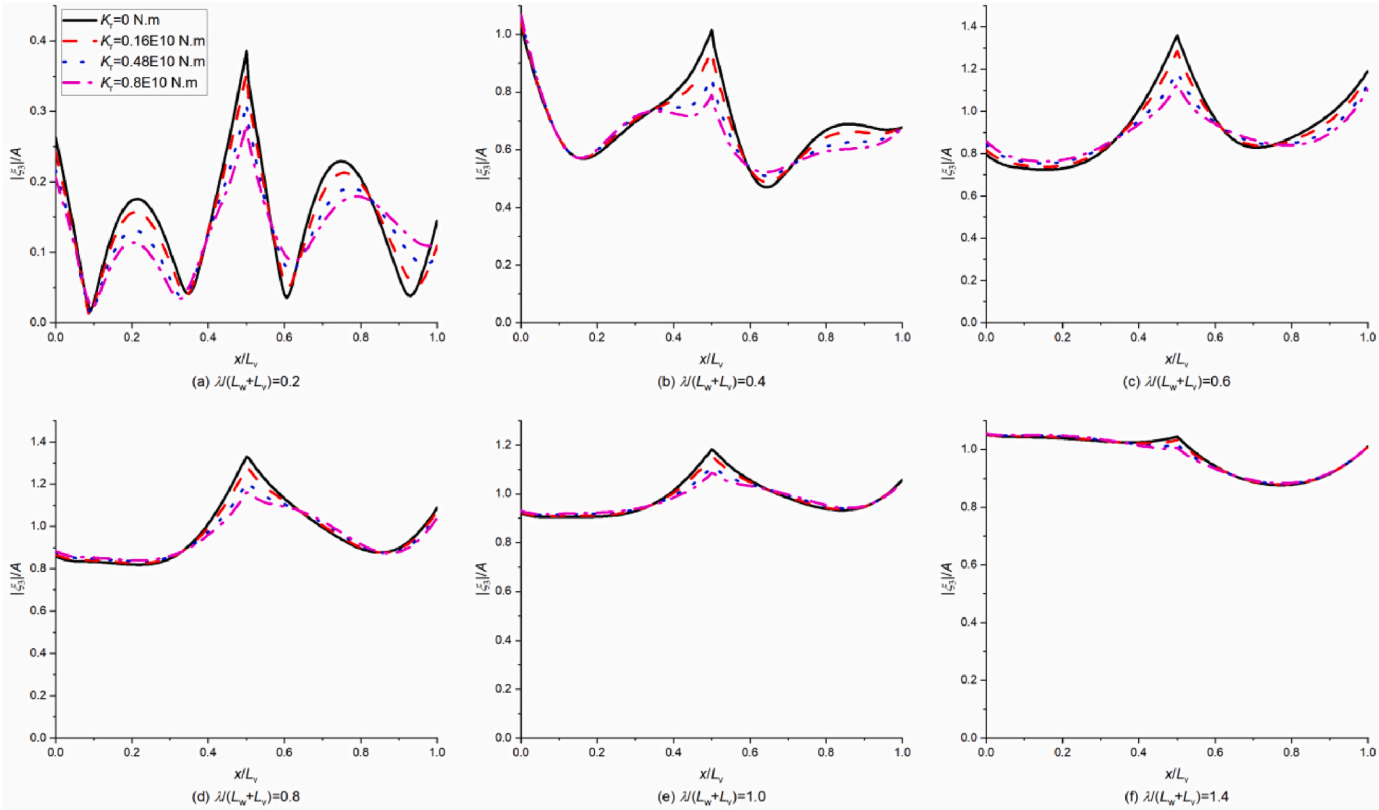

Fig. 12. Vertical displacement of the VLFS under different hinge rotational stiffness conditions.

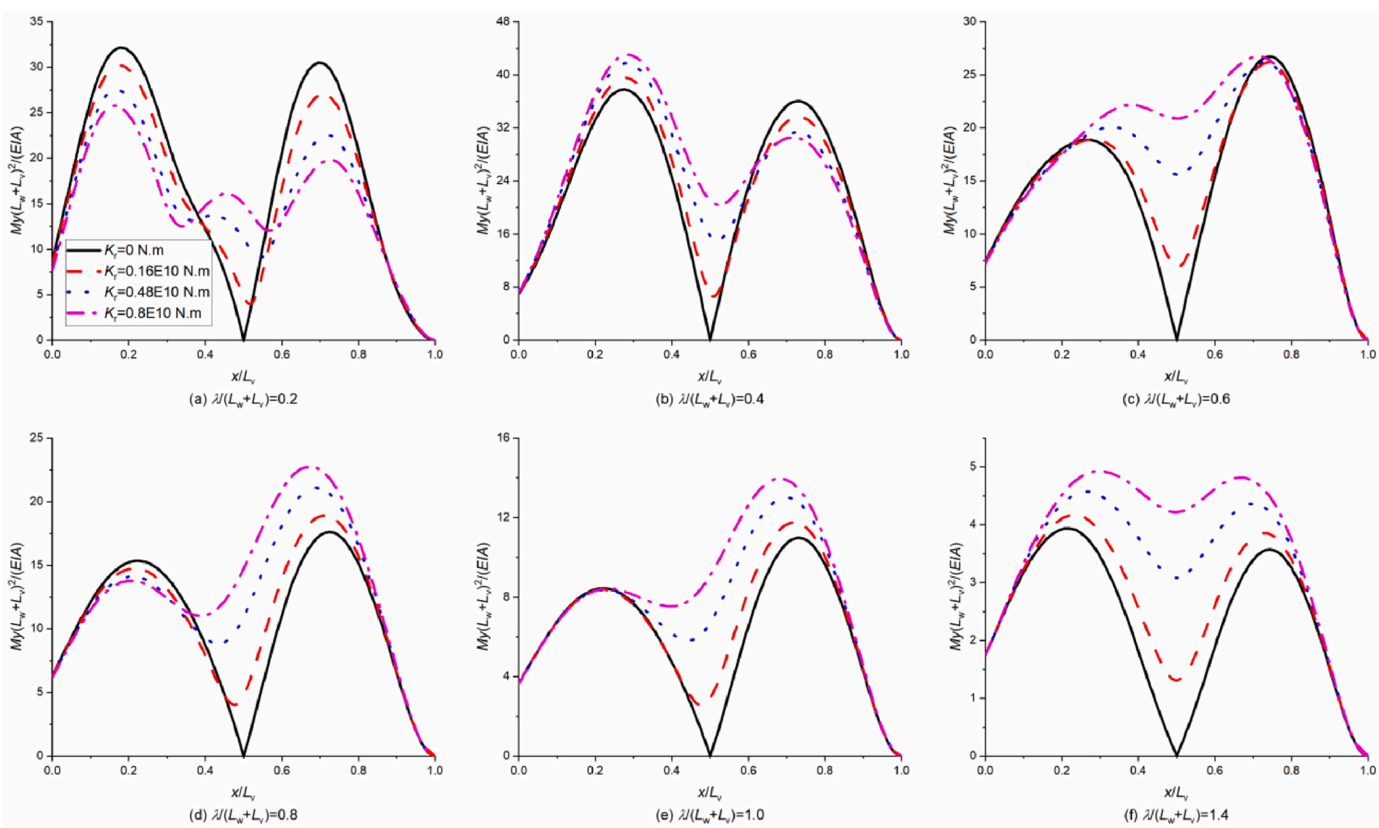

Fig. 13. Vertical bending moment of the VLFS under different hinge rotational stiffness conditions.

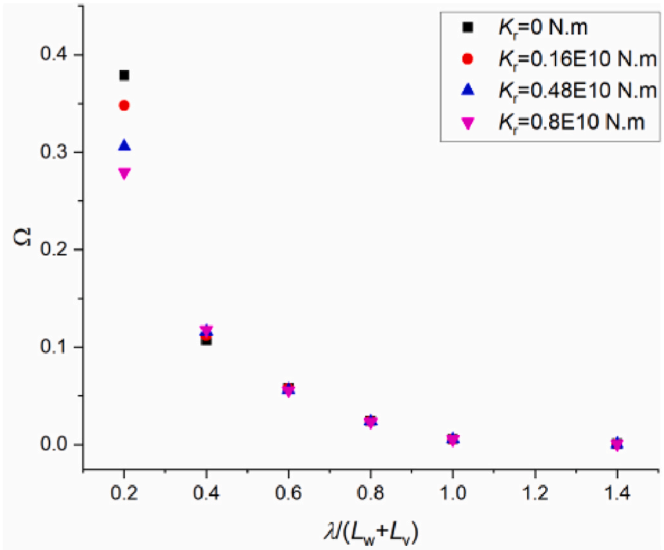

Fig. 14. CWR of the WEC under different hinge rotational stiffness conditions.

approaches or exceeds the structural scale ($\lambda/(L_w + L_v) = 1.0$ and 1.4), the overall shape of the bending moment distribution remains nearly unchanged for different rotational stiffness values. However, the bending moment amplitude still increases with increasing rotational stiffness. This suggests that larger rotational stiffness makes the structural behavior closer to that of a continuous system, thereby enhancing the global bending internal forces.

Fig. 14 presents the CWR of the WEC under different hinge rotational stiffness conditions. Overall, the hinge rotational stiffness has a certain influence on the WEC capture efficiency; however, this effect is primarily significant under short-wave conditions and gradually diminishes as the wavelength increases. Under short-wave conditions ($\lambda/(L_w + L_v) \leq 0.4$), the CWR is relatively high, and it slightly decreases with increasing hinge rotational stiffness. This is because a larger rotational stiffness constrains the overall deformation of the VLFS, thereby reducing the relative motion amplitude around the hinge of the PTO system. As the wavelength increases ($\lambda/(L_w + L_v) \geq 0.6$), the CWR decreases rapidly, and the differences among various rotational stiffness conditions become negligible. This indicates that, under long-wave conditions, the system motion is dominated by entire vertical motion, and the relative motion between the VLFS and WEC is significantly reduced. As a result, the influence of hinge rotational stiffness on the CWR becomes insignificant.

4.4. Effects of hinge location

Fig. 15 illustrates the vertical displacement of the VLFS under different hinge location conditions. At short-wave wavelengths ($\lambda/(L_w + L_v) = 0.2$ and 0.4), the structural displacement exhibits pronounced local oscillations along the length direction, due to the strong spatial variation of short waves acting on the structure. When the hinge is deployed at the midspan of the VLFS, the fore and aft modules can undergo significant relative rotation about this point, thereby amplifying local deformation and resulting in larger displacement amplitudes. In contrast, when the hinge is positioned closer to the fore or aft ends, the rotational interaction between modules has a weaker influence on the overall response, leading to relatively smaller displacement variations. As the wavelength increases ($\lambda/(L_w + L_v) = 0.6$ and 0.8), the displacement response gradually transitions from local oscillations to module-scale global deformation. Within this wavelength range, the hinge location alters the deformation pattern, causing displacement peaks to appear in different regions of the structure. When the hinge is located at the midspan, the structure is more likely to develop a symmetric bending

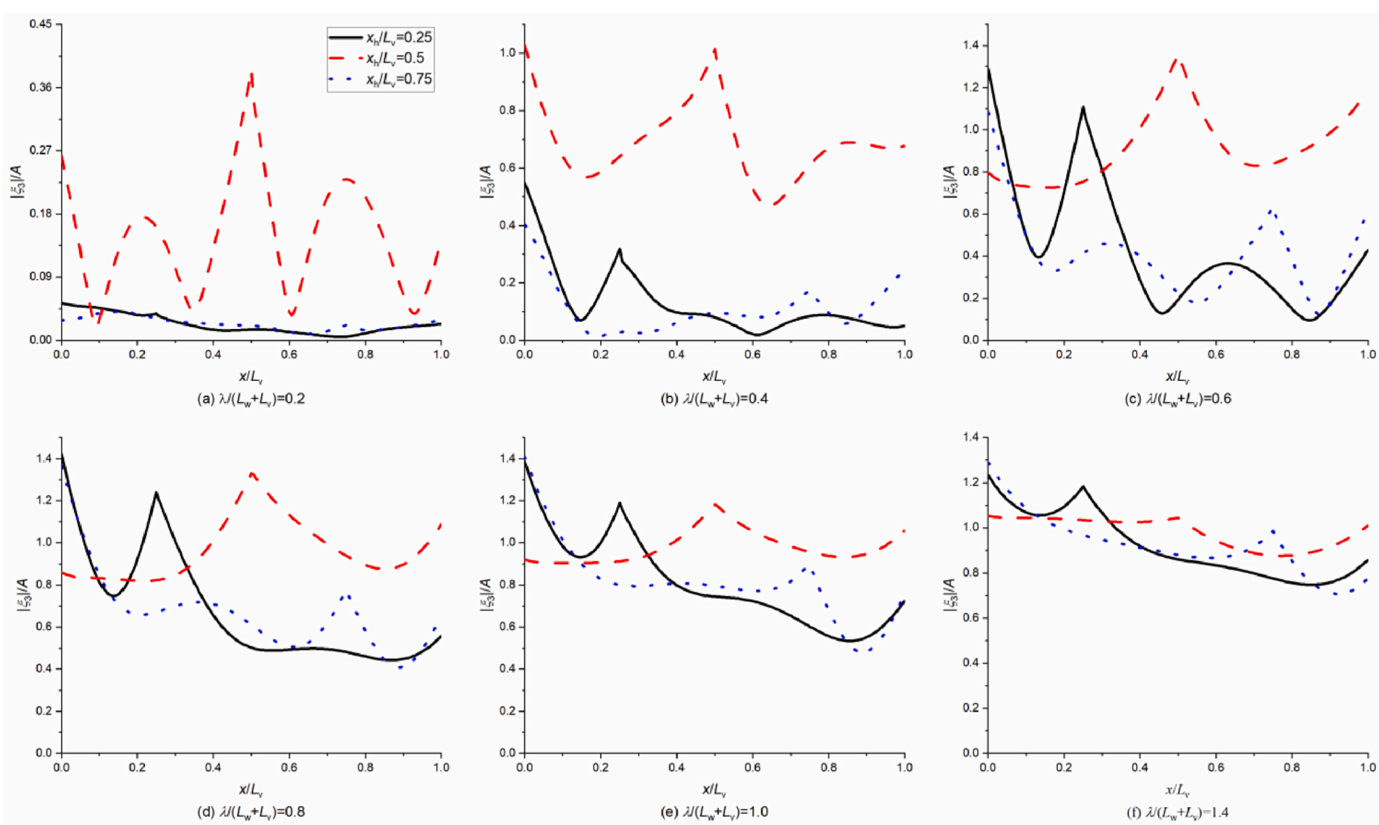

Fig. 15. Vertical displacement of the VLFS under different hinge location conditions.

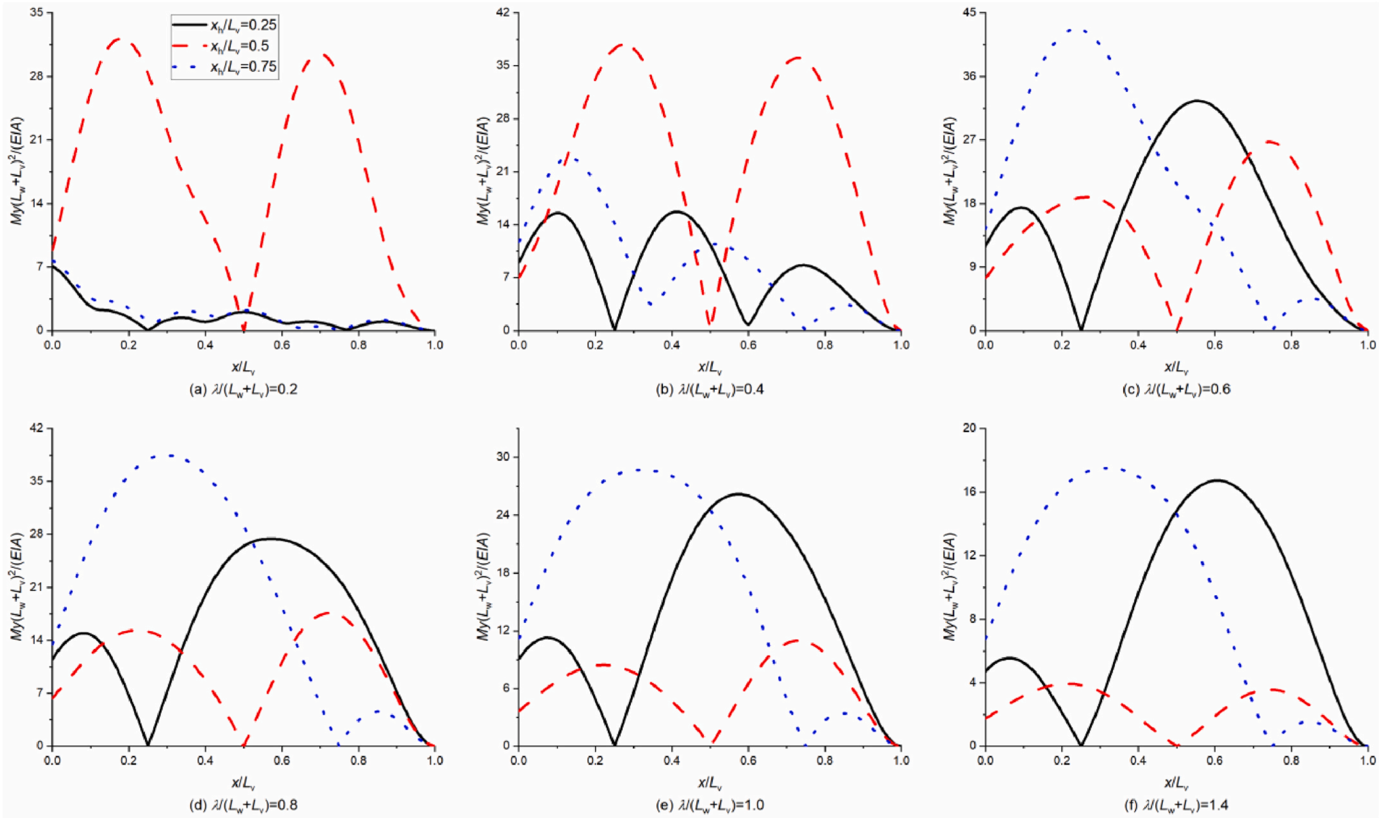

Fig. 16. Vertical bending moment of the VLFS under different hinge location conditions.

mode, resulting in larger displacement responses. When the wavelength is comparable to or greater than the structural scale ($\lambda/(L_w + L_v) = 1.0$ and 1.4), the structural motion becomes increasingly dominated by entire vertical motion, and spatial deformation diminishes. Consequently, the differences in displacement among various hinge location conditions become negligible.

Fig. 16 shows the vertical bending moments of the VLFS under different hinge location conditions. At short-wave wavelengths ($\lambda/(L_w + L_v) = 0.2$ and 0.4), the bending moment exhibits pronounced local variations along the structural length. Different hinge locations modify the spatial distribution of structural bending deformation, leading to noticeable differences in both the positions and amplitudes of bending moment peaks. When the hinge is deployed at the midspan of the VLFS, the two modules have comparable lengths, making it easier for the structure to develop a symmetric bending mode and thus resulting in larger bending moment responses. As the wavelength increases ($\lambda/(L_w + L_v) \geq 0.6$), the bending moment distribution gradually develops two dominant peaks, located at the middle of each module, while the bending moment at the hinge remains minimal. When the hinge deviates from the structural center, the asymmetry in module lengths becomes more pronounced, causing the bending moment peak to be more significant in the longer module.

Fig. 17 shows the CWR of the WEC under different hinge location conditions. Overall, for most wavelength cases, a hinge position at $x_h/L_v = 0.75$ yields relatively higher CWR. For $\lambda/(L_w + L_v) = 0.2$, the WEC achieves the highest CWR when the hinge is deployed at the middle position of the VLFS, whereas the CWR for $x_h/L_v = 0.25$ and 0.75 is nearly identical. This is because, compared with the cases of $x_h/L_v = 0.25$ and 0.75, deploying the hinge at the midspan results in more pronounced global deformation of the structure at this wavelength, thereby increasing the relative motion amplitude between the VLFS front end and the WEC. For $\lambda/(L_w + L_v) = 0.4$, the CWR reaches its maximum when the hinge is deployed near the aft part of the VLFS ($x_h/L_v = 0.75$). This indicates that the hinge location alters the deformation mode of the VLFS, which in turn affects the motion response at the front end and consequently influences the relative motion of the VLFS and WEC. As the wavelength further increases ($\lambda/(L_w + L_v) \geq 0.6$), the CWR decreases rapidly, and the differences among various hinge locations gradually diminish. This is because, under long-wave conditions, the VLFS and the WEC increasingly exhibit entire vertical motion, and thus the influence of hinge location on the CWR becomes insignificant.

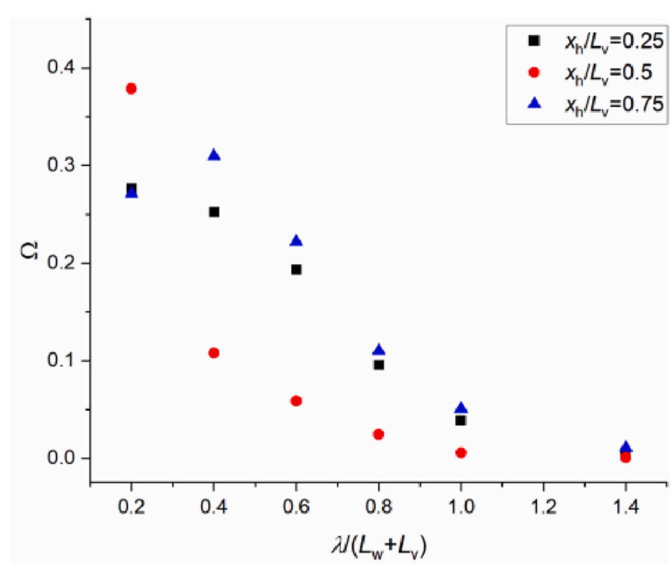

Fig. 17. CWR of the WEC under different hinge location conditions.

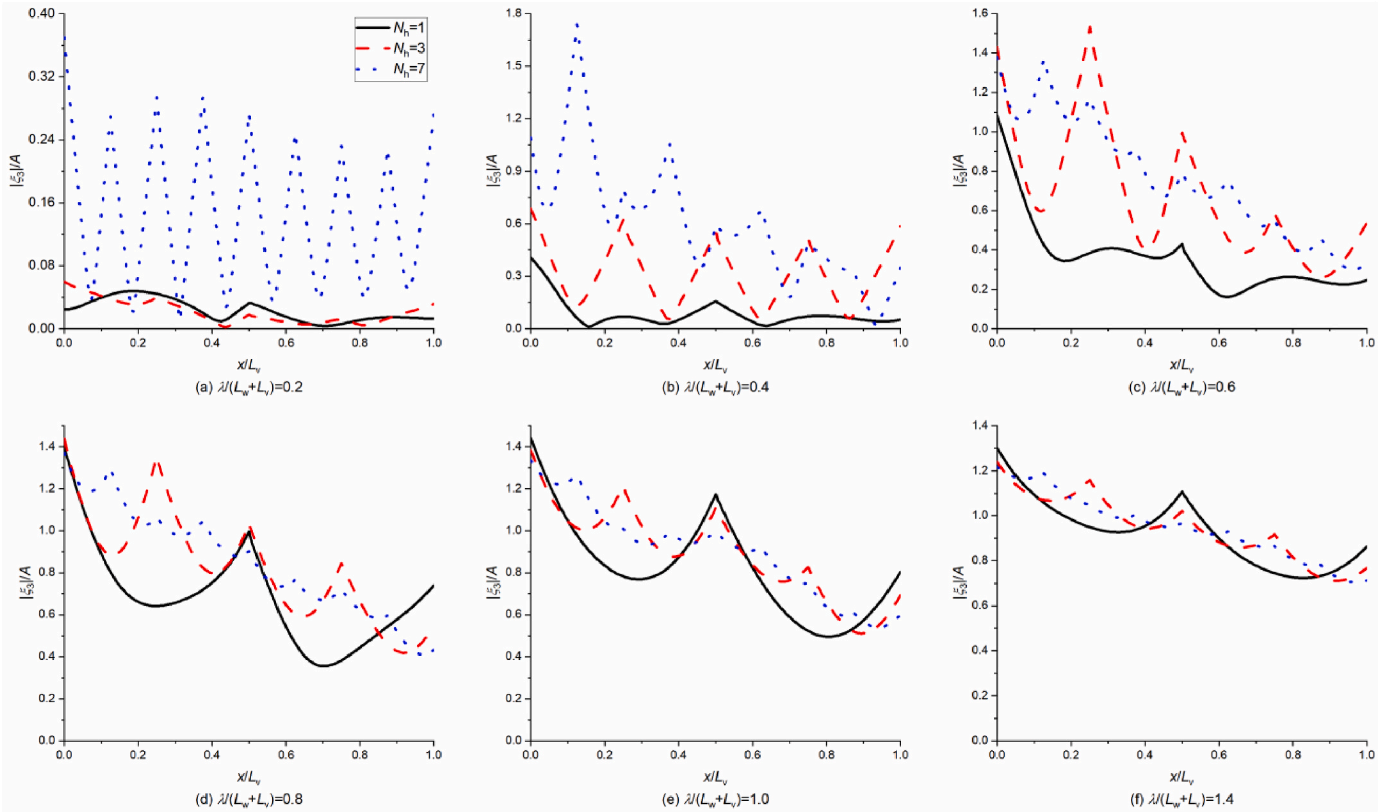

Fig. 18. Vertical displacement of the VLFS with different numbers of hinge.

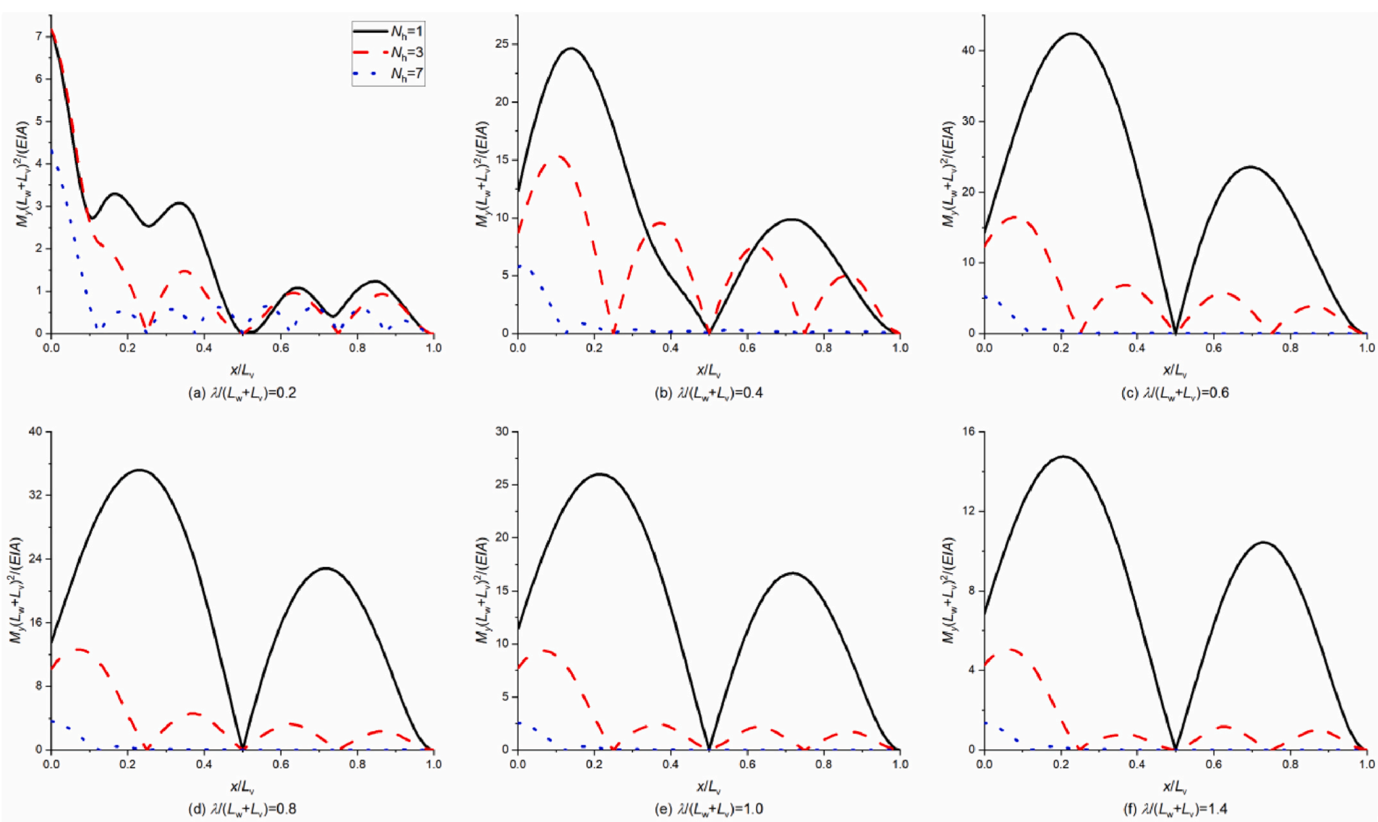

Fig. 19. Vertical bending moment of the VLFS with different numbers of hinge.

4.5. Effects of hinge number

Fig. 18 shows the vertical displacement of the VLFS with different numbers of hinge. At short-wave wavelengths ($\lambda/(L_w + L_v) = 0.2$ and 0.4), the displacement exhibits pronounced local oscillations along the structural length. As the number of hinges increases, the structure is divided into a greater number of relatively independent modules, which facilitates relative rotation between adjacent modules. This, in turn, enhances local deformation and leads to more significant variations in displacement. With increasing wavelength ($\lambda/(L_w + L_v) = 0.6$ and 0.8), the structural response gradually transitions from local oscillations to module-scale global deformation. At these wavelengths, the number of hinges continues to influence the deformation pattern, with a larger number of hinges resulting in a more distributed deformation and consequently altering the spatial distribution of displacement peaks. When the wavelength further approaches or exceeds the structural scale ($\lambda/(L_w + L_v) = 1.0$ and 1.4), the displacement curves corresponding to different hinge numbers become progressively smoother, and the differences among various cases are significantly reduced. This is because, under long-wave conditions, the structural motion is dominated by entire vertical motion, while local deformation is weakened; therefore, the effects of hinge number on the displacement response gradually diminish.

Fig. 19 illustrates the vertical bending moment of the VLFS with different hinge numbers. At short-wave wavelengths ($\lambda/(L_w + L_v) = 0.2$ and 0.4), noticeable differences in bending moments are observed among cases with different hinge numbers. When the number of hinges is small, the longer modules tend to develop larger bending moment responses under short-wave excitation. However, as the number of hinges increases, the structure is divided into more, shorter modules, allowing greater relative rotation between adjacent modules. This rotational flexibility effectively releases bending moments, resulting in a significant reduction in their amplitudes. As the wavelength further increases ($\lambda/(L_w + L_v) \geq 0.6$), the bending moment distribution under different hinge-number conditions becomes nearly identical in modal shape. The peak bending moments are primarily located at the midspan of each module. This indicates that, under intermediate-to-long wave conditions, the structural bending modes are predominantly governed by wave characteristics, whereas the number of hinges mainly influences the magnitude of bending moments without significantly altering their spatial distribution patterns.

Fig. 20 presents the CWR under different hinge number conditions. Overall, for most wavelengths, a smaller number of hinges leads to higher CWR. When $\lambda/(L_w + L_v) = 0.2$, the CWR increases with the number of hinges. This is because, at this wavelength, increasing the number of hinges enhances the local deformation capability of the VLFS, making the response at the front end more pronounced. Consequently, the relative motion of the WEC and the VLFS is amplified. However, for $\lambda/(L_w + L_v) > 0.2$, the CWR decreases as the number of hinges increases. This indicates that, with increasing wavelength, a larger number of hinges causes the structural deformation to become more distributed, thereby weakening the motion response at the front end and reducing the relative motion of the VLFS and WEC. As the wavelength further increases ($\lambda/(L_w + L_v) \geq 0.8$), the differences in CWR among different hinge-number conditions gradually diminish. This is because, under long-wave conditions, the VLFS and the WEC increasingly exhibit entire vertical motion, resulting in reduced relative motion between them. Consequently, the influence of hinge number on the CWR becomes insignificant.

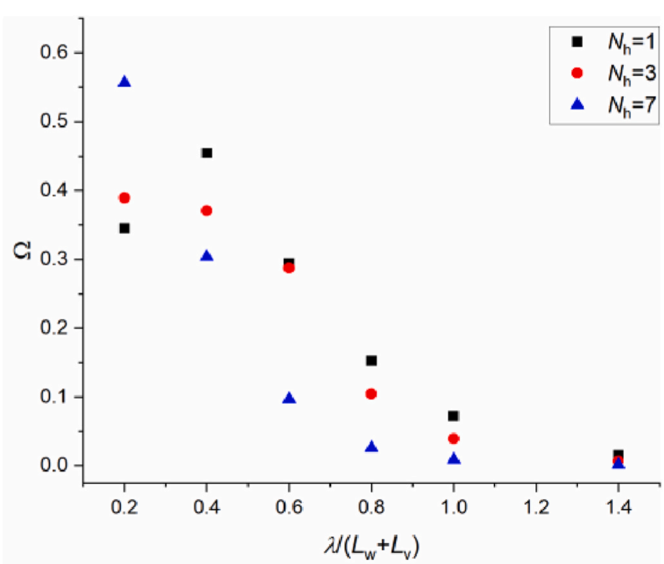

Fig. 20. CWR of the WEC under different hinge number conditions.

5. Conclusion

This paper presents a numerical study of the hydroelasticity and energy conversion of raft-type WEC-interconnected VLFS system. A hydroelastic analysis model based on the DMBB method is developed, and the motion equation for the coupled system is derived in the frequency domain. On this basis, a numerical search procedure is utilized to determine the optimal PTO damping. Subsequently, a parametric study is conducted using the established numerical model to examine the influence of wave and system properties on the deformation of the VLFS and power capture of the WEC. Based on the results, the main conclusions are summarized as follows.

(1) Under short-wave conditions, larger wave incident angles lead to increases in both the vertical displacement and bending moment of the VLFS, whereas under long-wave conditions, they result in larger displacement but smaller bending moment. In addition, under short-wave conditions, oblique waves may enhance the relative motion of the VLFS and WEC, thereby improving the capture efficiency, while under relatively long-wave conditions, the heading wave is more favorable for wave energy extraction.
(2) The structural flexibility exerts opposite effects on the displacement and bending moment responses of the VLFS. As the flexibility increases, the vertical displacement of the structure decreases significantly, whereas the bending moment increases markedly. Moreover, a smaller flexibility of the VLFS is beneficial for enhancing local deformation and improving the capture efficiency under short-wave conditions, while a larger flexibility is more advantageous for improving energy capture efficiency under intermediate-to long-wave conditions.
(3) A larger hinge rotational stiffness can reduce local displacement variations but increases the bending moment level. In addition, a smaller hinge rotational stiffness is more favorable under short-wave conditions for enhancing the relative rotation between the VLFS and WEC, thereby improving the capture efficiency. However, under long-wave conditions, the effects of hinge rotational stiffness on the energy capture efficiency are relatively limited.
(4) The hinge location not only alters the spatial distribution of vertical displacement of the VLFS but also affects the distribution characteristics of bending moments along the structural length, thereby exerting a significant influence on the hydroelastic response of the structure. Furthermore, increasing the number of hinges enhances local displacement variations, while effectively reducing the overall bending moment level of the structure.
(5) The hinge location and number influence the relative motion of the VLFS and WEC by altering the structural deformation modes and the motion characteristics of the VLFS fore end, thereby

affecting the WEC capture efficiency. This influence is more pronounced under short-to intermediate-wave conditions.

The WEC unit among the system not only captures wave energy to provide power supply for various facilities on the VLFS, but also functions in a manner analogous to a breakwater, thereby mitigating the deformation of the VLFS. It is noteworthy that this study is limited to the analysis of structural response and energy capture performance under regular wave conditions using a linear frequency-domain approach. For irregular wave conditions, time-domain analysis may be required to further account for the effects of nonlinear wave loads on the dynamic response of the system.

CRediT authorship contribution statement

Haitao Wu: Conceptualization, Data curation, Formal analysis, Investigation, Methodology, Validation, Visualization, Writing – original draft. **Laibing Jia:** Writing – review & editing. **Xiaosen Xu:** Writing – review & editing. **Wanru Deng:** Supervision, Writing – review & editing. **Zhiming Yuan:** Supervision, Writing – review & editing.

Declaration of competing interest

The authors declare that they have no known competing financial interests or personal relationships that could have appeared to influence the work reported in this paper.

Acknowledgement

The first author would like to thank Siqi Wu for the patience and support on his research.

Appendix A

Some related vectors and matrices in Section 2 can be expressed as:

$$\mathbf{M} = \begin{bmatrix} \mathbf{M}^{(1)} & \mathbf{M}^{(2)} & \ddots & \mathbf{M}^{(N_1+N_2+1)} \end{bmatrix}_{6(N_1+N_2+1)\times 6(N_1+N_2+1)} \tag{A1}$$

$$\mathbf{K}_{Hy} = \begin{bmatrix} \mathbf{C}^{(1)} & \mathbf{C}^{(2)} & \ddots & \mathbf{C}^{(N_1+N_2+1)} \end{bmatrix}_{6(N_1+N_2+1)\times 6(N_1+N_2+1)} \tag{A2}$$

where $\mathbf{M}^{(i)}$ and $\mathbf{C}^{(i)}$ denote the mass and hydrostatic stiffness matrices of the i-th body, respectively, both of which are of dimension 6×6.

$$\mathbf{M}^{(i)} = \begin{bmatrix} m^{(i)} & 0 & 0 & 0 & m^{(i)}z_g^{(i)} & 0 \\ 0 & m^{(i)} & 0 & -m^{(i)}z_g^{(i)} & 0 & m^{(i)}x_g^{(i)} \\ 0 & 0 & m^{(i)} & 0 & -m^{(i)}x_g^{(i)} & 0 \\ 0 & -m^{(i)}z_g^{(i)} & 0 & I_{44}^{(i)} & 0 & I_{46}^{(i)} \\ m^{(i)}z_g^{(i)} & 0 & -m^{(i)}x_g^{(i)} & 0 & I_{55}^{(i)} & 0 \\ 0 & m^{(i)}x_g^{(i)} & 0 & I_{64}^{(i)} & 0 & I_{66}^{(i)} \end{bmatrix} \tag{A3}$$

$$\mathbf{C}^{(i)} = \begin{bmatrix} 0 & 0 & 0 & 0 & 0 & 0 \\ 0 & 0 & 0 & 0 & 0 & 0 \\ 0 & 0 & \rho g A_w^{(i)} & 0 & -\rho g M_w^{(i)} & 0 \\ 0 & 0 & 0 & \rho g\left(I_{w1}^{(i)} + V^{(i)}z_b^{(i)}\right) & 0 & 0 \\ 0 & 0 & -\rho g M_w^{(i)} & 0 & \rho g\left(I_{w2}^{(i)} + V^{(i)}z_b^{(i)}\right) & 0 \\ 0 & 0 & 0 & 0 & 0 & 0 \end{bmatrix} \tag{A4}$$

where $m^{(i)}$ is the mass of the i-th body; $\left(x_g^{(i)}, y_g^{(i)}, z_g^{(i)}\right)$ denote the coordinates of the CoG; $I_{44}^{(i)}$, $I_{55}^{(i)}$, and $I_{66}^{(i)}$ are the moments of inertia corresponding to roll, pitch, and yaw DoFs, respectively; $I_{46}^{(i)} = I_{64}^{(i)}$ represents the coupled moment of inertia between roll and yaw DoFs; $A_w^{(i)}$ is the waterplane area; $M_w^{(i)}$ is the first moment of the waterplane area about the y-axis; $I_{w1}^{(i)}$ and $I_{w2}^{(i)}$ are the second moments of the waterplane area about the x- and y-axis, respectively; $V^{(i)}$ is the displaced volume; $z_b^{(i)}$ is the vertical coordinate of the center of buoyancy (CoB).

$$\mathbf{A}(\omega) = \begin{bmatrix} \mathbf{A}^{(1,1)} & \mathbf{A}^{(1,2)} & \cdots & \mathbf{A}^{(1,N_1+N_2+1)} \\ \mathbf{A}^{(2,1)} & \mathbf{A}^{(2,2)} & \cdots & \mathbf{A}^{(2,N_1+N_2+1)} \\ \vdots & \vdots & \ddots & \vdots \\ \mathbf{A}^{(N_1+N_2+1,1)} & \mathbf{A}^{(N_1+N_2+1,2)} & \cdots & \mathbf{A}^{(N_1+N_2+1,N_1+N_2+1)} \end{bmatrix}_{6(N_1+N_2+1)\times 6(N_1+N_2+1)} \tag{A5}$$

$$\mathbf{B}(\omega) = \begin{bmatrix} \mathbf{B}^{(1,1)} & \mathbf{B}^{(1,2)} & \cdots & \mathbf{B}^{(1,N_1+N_2+1)} \\ \mathbf{B}^{(2,1)} & \mathbf{B}^{(2,2)} & \cdots & \mathbf{B}^{(2,N_1+N_2+1)} \\ \vdots & \vdots & \ddots & \vdots \\ \mathbf{B}^{(N_1+N_2+1,1)} & \mathbf{B}^{(N_1+N_2+1,2)} & \cdots & \mathbf{B}^{(N_1+N_2+1,N_1+N_2+1)} \end{bmatrix}_{6(N_1+N_2+1)\times 6(N_1+N_2+1)} \tag{A6}$$

where $\mathbf{A}^{(i,j)}$ and $\mathbf{B}^{(i,j)}$ denote the added mass and radiation damping matrices of the i-th body induced by the motion of the j-th body, respectively, both of which are of dimension 6×6.

$$\boldsymbol{\xi} = \begin{bmatrix} \boldsymbol{\xi}^{(1)} \\ \boldsymbol{\xi}^{(2)} \\ \vdots \\ \boldsymbol{\xi}^{(N_1+N_2+1)} \end{bmatrix}_{6(N_1+N_2+1)\times 1} \tag{A7}$$

$$\mathbf{F}_E = \begin{bmatrix} \mathbf{F}_E^{(1)} \\ \mathbf{F}_E^{(2)} \\ \vdots \\ \mathbf{F}_E^{(N_1+N_2+1)} \end{bmatrix}_{6(N_1+N_2+1)\times 1} \tag{A8}$$

where $\mathbf{F}_E^{(i)} = \begin{bmatrix} F_{E,1}^{(i)} & F_{E,2}^{(i)} & F_{E,3}^{(i)} & F_{E,4}^{(i)} & F_{E,5}^{(i)} & F_{E,6}^{(i)} \end{bmatrix}^T$ denotes the wave excitation force acting on the i-th body.

$$\mathbf{K}_e = \begin{bmatrix}
\frac{EA_c}{l_e} & & & & & & & & & & & \text{symm.} \\
0 & \frac{12EI_z}{l_e^3} & & & & & & & & & & \\
0 & 0 & \frac{12EI_y}{l_e^3} & & & & & & & & & \\
0 & 0 & 0 & \frac{GI_x}{l_e} & & & & & & & & \\
0 & 0 & -\frac{6EI_y}{l_e^2} & 0 & \frac{4EI_y}{l_e} & & & & & & & \\
0 & \frac{6EI_z}{l_e^2} & 0 & 0 & 0 & \frac{4EI_z}{l_e} & & & & & & \\
-\frac{EA_c}{l_e} & 0 & 0 & 0 & 0 & 0 & \frac{EA_c}{l_e} & & & & & \\
0 & -\frac{12EI_z}{l_e^3} & 0 & 0 & 0 & -\frac{6EI_z}{l_e^2} & 0 & \frac{12EI_z}{l_e^3} & & & & \\
0 & 0 & -\frac{12EI_y}{l_e^3} & 0 & \frac{6EI_y}{l_e^2} & 0 & 0 & 0 & \frac{12EI_y}{l_e^3} & & & \\
0 & 0 & 0 & -\frac{GI_x}{l_e} & 0 & 0 & 0 & 0 & 0 & \frac{GI_x}{l_e} & & \\
0 & 0 & -\frac{6EI_y}{l_e^2} & 0 & \frac{2EI_y}{l_e} & 0 & 0 & 0 & \frac{6EI_y}{l_e^2} & 0 & \frac{4EI_y}{l_e} & \\
0 & \frac{6EI_z}{l_e^2} & 0 & 0 & 0 & \frac{2EI_z}{l_e} & 0 & -\frac{6EI_z}{l_e^2} & 0 & 0 & 0 & \frac{4EI_z}{l_e}
\end{bmatrix} \tag{A9}$$

where $\mathbf{K}_e$ is a 12×12 matrix; E and $G = \frac{E}{2(1+\nu)}$ are the Young's modulus and shear modulus, respectively, where ν denotes Poisson's ratio; l_e and A_c are the length and cross-sectional area of the beam, respectively; I_x, I_y, and I_z are the second moments of area about the x-, y-, and z-axis, respectively.

$$\mathbf{K}_{St} = \begin{bmatrix}
\overline{\mathbf{K}}_0^{(1,1)} + \mathbf{K}_1^{(1,1)} & \mathbf{K}_1^{(1,2)} & & & & & \\
\mathbf{K}_1^{(2,1)} & \mathbf{K}_1^{(2,2)} + \mathbf{K}_2^{(2,2)} & \mathbf{K}_{N_1-1}^{(N_1,N_1)} & \mathbf{K}_{N_1+2}^{(N_1+1,N_1+1)} & \mathbf{K}_{N_1+2}^{(N_1+1,N_1+2)} & & \\
 & \ddots & & \mathbf{K}_{N_1+2}^{(N_1+2,N_1+1)} & \mathbf{K}_{N_1+2}^{(N_1+2,N_1+2)} + \mathbf{K}_{N_1+3}^{(N_1+2,N_1+2)} & \ddots & \mathbf{K}_{N_1+N_2}^{(N_1+N_2,N_1+N_2)} + \overline{\mathbf{K}}_{N_1+N_2+1}^{(N_1+N_2,N_1+N_2)} & 0_{6(N_1+N_2)\times 6} \\
 & & & & 0_{6\times 6(N_1+N_2)} & & & 0_{6\times 6}
\end{bmatrix}_{6(N_1+N_2+1)\times 6(N_1+N_2+1)} \tag{A10}$$

where $\mathbf{K}_q^{(i,j)}(q=0,1,...,N_1\text{-}1;\ i=q \text{ or } q+1;\ j=q \text{ or } q+1)$ of the beam elements on module 1, and $\mathbf{K}_q^{(i,j)}(q=N_1+2,...,N_1+N_2;\ i=q\text{-}1 \text{ or } q;\ j=q\text{-}1 \text{ or } q)$ o f the beam elements on module 2, are all the submatrices of$\mathbf{K}_q$.

$$\overline{\mathbf{K}}_0^{(1,1)} = -\mathbf{K}_0^{(1,0)}\left[\mathbf{K}_0^{(0,0)}\right]^{-1}\mathbf{K}_0^{(0,1)} + \mathbf{K}_0^{(1,1)} \tag{A11}$$

$$\overline{\mathbf{K}}_{N_1+N_2+1}^{(N_1+N_2,N_1+N_2)} = -\mathbf{K}_{N_1+N_2+1}^{(N_1+N_2+1,N_1+N_2+2)}\left[\mathbf{K}_{N_1+N_2+1}^{(N_1+N_2+2,N_1+N_2+2)}\right]^{-1}\mathbf{K}_{N_1+N_2+1}^{(N_1+N_2+2,N_1+N_2+1)} + \mathbf{K}_{N_1+N_2+1}^{(N_1+N_2+1,N_1+N_2+1)} \tag{A12}$$

where $\overline{\mathbf{K}}_0^{(1,1)}$ denotes the equivalent stiffness submatrix exerted by beam element 0 on lumped mass 1; likewise, $\overline{\mathbf{K}}_{N_1+N_2+1}^{(N_1+N_2,N_1+N_2)}$ represents the equivalent stiffness submatrix exerted by beam element $N_1 + N_2 + 1$ on lumped mass $N_1 + N_2$.

$$\mathbf{C}_{\mathrm{pto}} = \begin{bmatrix} \overline{\mathbf{C}}_{\mathrm{pto}} & 0_{6\times6(\mathrm{N}_1+\mathrm{N}_2-1)} & -\overline{\mathbf{C}}_{\mathrm{pto}} \\ & 0_{(\mathrm{N}_1+\mathrm{N}_2-1)\times6(\mathrm{N}_1+\mathrm{N}_2+1)} & \\ -\overline{\mathbf{C}}_{\mathrm{pto}} & 0_{6\times6(\mathrm{N}_1+\mathrm{N}_2-1)} & \overline{\mathbf{C}}_{\mathrm{pto}} \end{bmatrix}_{6(\mathrm{N}_1+\mathrm{N}_2+1)\times6(\mathrm{N}_1+\mathrm{N}_2+1)} \tag{A13}$$

where the expression of $\overline{\mathbf{C}}_{\mathrm{pto}}$ is,

$$\overline{\mathbf{C}}_{\mathrm{pto}} = \begin{bmatrix} 0 & 0 & 0 & 0 & 0 & 0 \\ 0 & 0 & 0 & 0 & 0 & 0 \\ 0 & 0 & 0 & 0 & 0 & 0 \\ 0 & 0 & 0 & 0 & 0 & 0 \\ 0 & 0 & 0 & 0 & \mathrm{C}_p & 0 \\ 0 & 0 & 0 & 0 & 0 & 0 \end{bmatrix} \tag{A14}$$

$$\mathbf{K}_{\mathrm{Rot}} = \begin{bmatrix} & 0_{6(\mathrm{N}_1-1)\times6(\mathrm{N}_1+\mathrm{N}_2+1)} & & \\ 0_{6\times6(\mathrm{N}_1-1)} & \overline{\mathbf{K}}_{\mathrm{Rot}} & -\overline{\mathbf{K}}_{\mathrm{Rot}} & 0_{6\times6\mathrm{N}_2} \\ 0_{6\times6(\mathrm{N}_1-1)} & -\overline{\mathbf{K}}_{\mathrm{Rot}} & \overline{\mathbf{K}}_{\mathrm{Rot}} & 0_{6\times6\mathrm{N}_2} \\ & 0_{6\mathrm{N}_2\times6(\mathrm{N}_1+\mathrm{N}_2+1)} & & \end{bmatrix}_{6(\mathrm{N}_1+\mathrm{N}_2+1)\times6(\mathrm{N}_1+\mathrm{N}_2+1)} \tag{A15}$$

where $\overline{\mathbf{K}}_{\mathrm{Rot}}$ can be expressed as:

$$\overline{\mathbf{K}}_{\mathrm{Rot}} = \begin{bmatrix} 0 & 0 & 0 & 0 & 0 & 0 \\ 0 & 0 & 0 & 0 & 0 & 0 \\ 0 & 0 & 0 & 0 & 0 & 0 \\ 0 & 0 & 0 & 0 & 0 & 0 \\ 0 & 0 & 0 & 0 & \mathrm{K}_r & 0 \\ 0 & 0 & 0 & 0 & 0 & 0 \end{bmatrix} \tag{A16}$$

where K_r is the hinge rotational stiffness coefficient.

References

Andrianov, A.I., Hermans, A.J., 2003. The influence of water depth on the hydroelastic response of a very large floating platform. Mar. Struct. 16 (5), 355–371.

Belibassakis, K.A., Athanassoulis, G.A., 2005. A coupled-mode model for the hydroelastic analysis of large floating bodies over variable bathymetry regions. J. Fluid Mech. 531, 221–249.

Chen, Y., Zhang, X., Liu, L., Tian, X., Li, X., Cheng, Z., 2023. A discrete-module finite-element hydroelasticity method in analyzing dynamic response of floating flexible structures. J. Fluid Struct. 117, 103825.

Chen, Y., Zhang, X., Tian, X., Guo, X., Li, X., Zhang, X., 2022. A numerical framework for hydroelastic analysis of a flexible floating structure under unsteady external excitations: motion and internal force/moment. Ocean Eng 253, 111288.

Cheng, Y., Ji, C., Zhai, G., Oleg, G., 2016. Dual inclined perforated anti-motion plates for mitigating hydroelastic response of a VLFS under wave action. Ocean Eng 121, 572–591.

Cheng, Y., Song, F., Xi, C., Collu, M., Yuan, Z., Incecik, A., 2023. Feasibility of integrating a very large floating structure with multiple wave energy converters combining oscillating water columns and oscillating flaps. Energy 274, 127301.

Diamantoulaki, I., Angelides, D.C., Manolis, G.D., 2008. Performance of pile-restrained flexible floating breakwaters. Appl. Ocean Res. 30, 243–255.

Fu, S., Moan, T., Chen, X., Cui, W., 2007. Hydroelastic analysis of flexible floating inter-connected structures. Ocean Eng 34 (11–12), 1516–1531.

Gao, R.P., Tay, Z.Y., Wang, C.M., Koh, C.G., 2011. Hydroelastic response of very large floating structure with a flexible line connection. Ocean Eng 38, 1957–1966.

Hong, D.C., Hong, S.Y., Hong, S.W., 2006. Reduction of hydroelastic responses of a very-long floating structure by a floating oscillating-water-column breakwater system. Ocean Eng 33 (5–6), 610–634.

Jin, C., Lee, I., Bakti, F., Kim, D.K., Kim, S., Kim, M., 2025. Multi-body-based 2D hydroelasticity simulations in time domain for moored floating structure. Eng. Struct. 329, 119789.

Karmakar, D., Guedes Soares, C., 2012. Scattering of gravity waves by a moored finite floating elastic plate. Appl. Ocean Res. 34, 135–149.

Karperaki, A.E., Belibassakis, K.A., Papathanasiou, T.K., 2016. Time-domain, shallow-water hydroelastic analysis of VLFS elastically connected to the seabed. Mar. Struct. 48, 33–51.

Kashiwagi, M., 2000. A time-domain mode-expansion method for calculating transient elastic responses of a pontoon-type VLFS. J. Mar. Sci. Technol. 5 (2), 89–100.

Kim, B., Hong, S., Kyoung, J., Cho, S., 2007. Evaluation of bending moments and shear forces at unit connections of very large floating structures using hydroelastic and rigid body analyses. Ocean Eng 34 (11–12), 1668–1679.

Kim, B., Kyoung, J., Hong, S., Cho, S., 2005. Investigation of the effect of stiffness distribution and structure shape on hydroelastic responses of very large floating structures. In: Proc. 15th Int. Offshore Polar. Eng. Conf., pp. 210–217

Lamas-Pardo, M., Iglesias, G., Carral, L., 2015. A review of very large floating structures (VLFS) for coastal and offshore uses. Ocean Eng 109, 677–690.

Loukogeorgaki, E., Michailides, C., Angelides, D.C., 2012. Hydroelastic analysis of a flexible mat-shaped floating breakwater under oblique wave action. J. Fluid Struct. 31, 103–124.

Lu, D., Fu, S., Zhang, X., Guo, F., Gao, Y., 2019. A method to estimate the hydroelastic behaviour of VLFS based on multi-rigid-body dynamics and beam bending. Ships Offshore Struct. 14 (4), 354–362.

Michailides, C., Loukogeorgaki, E., Angelides, D.C., 2013. Response analysis and optimum configuration of a modular floating structure with flexible connectors. Appl. Ocean Res. 43, 112–130.

Nguyen, H.P., Liang, H., Luong, V.H., 2023. Finite element–dual boundary element method for hydroelastic analysis of very large floating structures protected by perforated barrier. Ocean Eng 268, 113511.

Nguyen, H.P., Wang, C.M., Flocard, F., Pedroso, D.M., 2019. Extracting energy while reducing hydroelastic responses of VLFS using a modular raft WEC-type attachment. Appl. Ocean Res. 84, 302–316.

Nguyen, H.P., Wang, C.M., 2020. Heaving wave energy converter-type attachments to a pontoon-type very large floating structure. Eng. Struct. 219, 110964.

Papathanasiou, T.K., Karperaki, A., Theotokoglou, E.E., Belibassakis, K.A., 2015. A higher-order FEM for time-domain hydroelastic analysis of large floating bodies in an inhomogeneous shallow water environment. Proc. R. Soc. A 471 (2173), 20140643.

Pham, D.C., Wang, C.M., Utsunomiya, T., 2008. Hydroelastic analysis of pontoon-type circular VLFS with an attached submerged plate. Appl. Ocean Res. 30, 287–296.

Riyansyah, M., Wang, C.M., Choo, Y.S., 2010. Connection design for two-floating beam system for minimum hydroelastic response. Mar. Struct. 23, 67–87.

Senjanović, I., Malenica, Š., Tomas, S., 2008. Investigation of ship hydroelasticity. Ocean Eng 35 (5–6), 523–535.

Shi, Y., Wei, Y., Chen, Z., 2024. Development of reduced-order discrete-module method for hydroelastic analysis of floating flexible structures. J. Fluid Struct. 130, 104188.

Shi, Y., Wei, Y., Tay, Z.Y., Chen, Z., 2023. Hydroelastic analysis of offshore floating photovoltaic based on frequency-domain model. Ocean Eng 289, 116213.

Sun, L., Taylor, R.E., Choo, Y.S., 2011. Responses of interconnected floating bodies. IES J. Part A Civ. Struct. Eng. 4, 143–156.
Sun, Y., Lu, D., Xu, J., Zhang, X., 2018. A study of hydroelastic behavior of hinged VLFS. Int. J. Nav. Archit. Ocean Eng. 10 (2), 170–179.
Tan, L., Tang, G.Q., Zhou, Z.B., Cheng, L., Chen, X., Lu, L., 2017. Theoretical and numerical investigations of wave resonance between two floating bodies in close proximity. J. Hydrodyn. B 29 (5), 805–816.
Tay, Z.Y., 2025. Raft-type modular articulated plate for offshore floating photovoltaic farms: antimotion performance and wave energy conversion. Ships Offshore Struct. 1–28. https://doi.org/10.1080/17445302.2025.2588146.
Tay, Z.Y., Wang, C.M., 2012. Reducing hydroelastic response of very large floating structures by altering their plan shapes. Ocean Syst. Eng. 2, 69–81.
Taylor, E.R., 2007. Hydroelastic analysis of plates and some approximations. J. Eng. Math. 58 (1), 267–278.
Tuitman, J.T., Malenica, Š., Van't Veer, R., 2012. Generalized modes in time-domain seakeeping calculations. J. Ship Res. 56 (4), 215–233.
Wang, C.M., Tay, Z.Y., Takagi, K., Utsunomiya, T., 2010. Literature review of methods for mitigating hydroelastic response of VLFS under wave action. Appl. Mech. Rev. 63 (3), 030802.
Wu, H., Yuan, Z., 2026a. Influence of WEC geometric variables on the performance of an integrated WEC–VLFS system. Ocean Eng 352, 124470.
Wu, H., Yuan, Z., 2026b. Performance investigation of an oscillating-body WEC with the tristable energy capture mechanism. Ocean Eng 343, 123538.
Xu, J., Sun, Y., Li, Z., Zhang, X., Lu, D., 2017. Analysis of the hydroelastic performance of very large floating structures based on multimodules beam theory. Math. Probl Eng. 2017, 6482527.
Yoon, J., Cho, S., Jiwinangun, R., Lee, P., 2014. Hydroelastic analysis of floating plates with multiple Hinge connections in regular waves. Mar. Struct. 36, 65–87.
Zhang, X., Zheng, S., Lu, D., Tian, X., 2019. Numerical investigation of the dynamic response and power capture performance of a VLFS with a wave energy conversion unit. Eng. Struct. 195, 62–83.
Zhang, Z., Dai, L., Wang, Z., Wu, H., 2026. Effects of WEC geometry on the performance of WEC array–VLFS integrated system. Pol. Marit. Res. 33 (1), 63–73.
Zhang, X., Lu, D., 2018. An extension of a discrete-module-beam-bending-based hydroelasticity method for a flexible structure with complex geometric features. Ocean Eng 163, 22–28.
Zhao, C., Zhang, J., Huang, W., 2007. Vibration reduction of floating elastic plates in water waves. Mar. Struct. 20, 71–99.
Zhao, X., Wang, J., Zhou, Y., Zhang, L., Geng, J., 2026. Hydrodynamic analysis of a very large floating structure coupled with an array of wave energy converters. Eng. Struct. 357, 122487.
Zhao, X., Xue, F., Chen, L., Göteman, M., Han, D., Geng, J., Sun, S., 2023. Hydrodynamic analysis of a floating platform coupled with an array of oscillating bodies. Ocean Eng 287, 115439.
Zheng, S., Zhang, Y., Sheng, W., 2015. Numerical study on the dynamics of a two-raft wave energy conversion device. J. Fluid Struct. 58, 271–290.